ON-CHIP OPTICAL STABILIZATION OF HIGH-SPEED MODE-LOCKED QUANTUM DOT LASERS FOR NEXT GENERATION OPTICAL NETWORKS

by

ABHIJEET DILIP ARDEY
B.S. University of Delhi, 2001
M.S. University of Delhi, 2003
M.S. University of Central Florida, 2007

A dissertation submitted in partial fulfillment of the requirements
for the degree of Doctor of Philosophy
in the Department of Physics
in the College of Sciences
at the University of Central Florida
Orlando, Florida

Summer Term
2014

Major Professor: Peter J. Delfyett, Jr.

ABSTRACT

Monolithic passively mode-locked colliding pulse semiconductor lasers generating pico- to sub-picosecond terahertz optical pulse trains are promising sources for future applications in ultra-high speed data transmission systems and optical measurements. However, in the absence of external synchronization, these passively mode-locked lasers suffer from large amplitude and timing jitter instabilities resulting in broad comb linewidths, which precludes many applications in the field of coherent communications and signal processing where a much narrower frequency line set is needed.

In this dissertation, a novel quantum dot based coupled cavity laser is presented, where for the first time, four-wave mixing (FWM) in the monolithically integrated saturable absorber is used to injection lock a monolithic colliding pulse mode-locked (CPM) laser with a mode-locked high-Q ring laser. Starting with a passively mode-locked master ring laser, a stable 30 GHz optical pulse train is generated with more than 10 dB reduction in the RF noise level at 20 MHz offset and close to 3-times reduction in the average optical linewidth of the injection locked CPM slave laser. The FWM process is subsequently verified experimentally and conclusively shown to be the primary mechanism responsible for the observed injection locking. Other linear scattering effects are found to be negligible, as predicted in the orthogonal waveguide configuration. The novel injection locking technique is further exploited by employing optical hybrid mode-locking and increasing the Q of the master ring cavity, to realize an improved stabilization architecture. Dramatic reduction is shown with more than 14-times reduction in the photodetected beat linewidth and almost 5-times reduction in the optical linewidth of the injection locked slave laser with generation of close to transform limited pulses at ~ 30 GHz. These results demonstrate

the effectiveness of the novel injection locking technique for an all-on-chip stability transfer and provides a new way of stabilizing monolithic optical pulse sources for applications in future high speed optical networks.

This work is dedicated to my family for their constant support and unconditional love.

ACKNOWLEDGMENTS

I would like to thank my advisor, Prof. Peter Delfyett who believed in me and without whose support none of what follows would have been possible. His patience, motivation and enthusiasm guided me through the most difficult times while writing my dissertation. I could not have imagined a better advisor and mentor for my Ph.D. study.

I would also like to thank the entire Ultrafast Photonics group, members past and present, for their support that helped make this work possible. They are Dr. Sangyoun Gee, Dr. Franklyn Quinlan, Dr. Sarper Ozharar, Dr. Jimyung Kim, Dr. Ibrahim Ozdur, Dr. Dimitrios Mandridis, Dr. Mohammad Umar Piracha, Dr. Mehmetcan Akbulut, Dr. Nishant Bhatambrekar, Dr. Nazanin Hoghooghi, Dr. Josue Davila-Rodriguez, Dr. Charles Williams, Dr. Dat Nguyen, Sharad Bhooplapur, Marcus Bagnell, Edris Sarailou, Anthony Klee and Kristina Bagnell.

TABLE OF CONTENTS

LIST OF FIGURES

LIST OF TABLES

LIST OF ACRONYMS/ABBREVIATIONS

AR	Anti-Reflection
AOM	Acousto-Optic Modulator
ASE	Amplified Spontaneous Emission
BCB	Benzocyclobutene
BS	Beam Splitter
CPM	Colliding Pulse Mode-locked laser
CW	Continuous Wave
EAM	Electro-absorption modulator
FP	Fabry-Pérot
FSR	Free Spectral Range
FWM	Four-Wave Mixing
ISO	Optical Isolator
IV	Current output Versus Voltage
LEF	Linewidth Enhancement Factor
LI	Light output Versus Current
MZI	Mach-Zehnder Interferometer
OTDM	Optical Time-Division Multiplexing
PBS	Polarizing Beam Splitter
PC	Polarization Controller
PD	Photodetector
PECVD	Plasma Enhanced Chemical Vapor Deposition
POL	Polarizer

QD	Quantum Dot
QW	Quantum Well
RF	Radio Frequency
RIE	Reative-ion Etching
RTA	Rapid Thermal Annealing
SA	Saturable Absorber
SEM	Scanning Electron Microscope
SMF	Single Mode Fiber
SOA	Semiconductor Optical Amplifier
SOI	Silicon on Insulator
TBP	Time-Bandwidth Product
TE	Transverse Electric
TEC	Thermo-Electric Cooler
UV	Ultraviolet

CHAPTER 1
INTRODUCTION

Light sources generating short optical pulses at high repetition frequencies are the key components for future large capacity optical communication networks. These include high-bit-rate optical time-division multiplexing (OTDM) systems and microwave & millimeter-wave photonic systems [1], [2]. Infact lasers operating at tens of gigahertz repetition rates are already being implemented in high-capacity telecommunication systems, photonics switching devices and clocks for very-large-scale integrated microprocessors. High-frequency short optical pulses generated are also being used for ultrafast optical measurements, such as electro-optic sampling and optical analogue to digital conversion. In recent years, monolithic mode-locked semiconductor lasers have attracted considerable attention for these photonic applications. These mechanically stable and cost-effective laser diodes have excellent pulse characteristics over other optical pulse sources including high repetition rates, short pulsewidths and small frequency chirp. Monolithic passively mode-locked lasers, especially quantum dot (QD) based lasers with unique characteristics, such as ultrabroad gain bandwidth, low threshold current, enhanced temperature stability, low linewidth enhancement factor, and ultrafast gain and absorption dynamics offer promise as compact, reliable and robust optical sources [3-5]. However, in the absence of direct electrical modulation, these passively mode-locked lasers are susceptible to large amplitude and timing jitter instabilities resulting in broad comb linewidths, which precludes many applications in the field of coherent communications and signal processing where a much narrower frequency line set is needed [6], [7]. Previous research has been focused on the external stabilization of pulse trains such as optoelectronic

feedback using phase-locked loops, optical pulse injection, and sub-harmonic optical injection [8-10]. Recently, optical micro-resonators have also been demonstrated to serve as compact sources of optical frequency combs [11]. However, the complexity of all these techniques, and the fabrication and cost involved, limit their applications.

In this Ph.D. dissertation, we present a novel and simple QD based multi-section laser design where a stable high-Q passively mode-locked ring laser is used to injection lock a passively mode-locked colliding pulse mode-locked (CPM) laser. CPM laser design using an intracavity saturable absorber is chosen as it provides nearly transform limited ultrafast optical pulse train without the need for high speed electronics. These lasers have already been demonstrated to produce pico- to sub-picosecond pulses at repetition frequencies from 16 to 480 GHz [12], [13]. Owing to the sparse nature of the QD material, which results in low modal gain, the colliding pulse design is optimal as it avoids the need for the impractical shortening of cavity length. In the novel laser design demonstrated, four-wave mixing (FWM) in the common saturable absorber is used for injection locking, which stabilizes and hence reduces the timing jitter as well as the long-term frequency drift of the slave laser. A stable 30 GHz optical pulse train is generated and both the RF and optical linewidths are significantly reduced confirming the effectiveness of the FWM technique. This is the first time, to the best of our knowledge that FWM has been conclusively shown to be used for injection locking in semiconductor media especially in an orthogonal waveguide configuration. We also subsequently investigate the contributions from other mechanisms such as linear scattering, which are found to be negligible as expected in the case of low-index contrast perpendicular waveguide crossings. Finally we show that by hybrid mode-locking the external ring cavity laser and decreasing the losses

in the high-Q cavity, the jitter values of the injected slave laser can be further reduced making this ultra-compact and ultra-short optical pulse source attractive for use in the forthcoming photonic access networks.

1.1 Mode-locked lasers

Short optical pulse diode lasers have been proposed using a wide range of schemes such as gain switching, Q-Switching and mode-locking [14]. Gain switched and Q-switched lasers are attractive since they do not require external cavities, are easy to operate and have the flexibility of changing cavity repetition rate without modifying the cavity length. However, they exhibit significant frequency chirp and timing jitter coupled with wide pulsewidths and large time-bandwidth products. Mode-locked semiconductor lasers facilitate short optical pulses with very pure spectral properties and low timing jitter [15]. In mode-locked lasers the pulse generation is through the phase locking of longitudinal modes supported by the cavity with the repetition rate of the pulse-train defined by the cavity length and the number of pulses circulating in the cavity. The monolithic cavity designs reported thus have repetition rates from 10 to in excess of hundreds of GHz depending on the cavity length and if whether harmonic mode-locking is implemented.

The simplest cavity configuration for mode-locking is the single-segment design where direct electrical modulation is used to generate accurately timed pulses by synchronizing the optical pulse train to systems clocks and also reduce the timing jitter. This scheme is referred to active mode-locking. A stable microwave oscillator can be used to modulate an intracavity gain, loss or phase element at the cavity round-trip frequency to lock the longitudinal modes of the laser and produce short optical pulses. However, as you can infer the optical pulse width in this case is determined by how narrow the electrical

modulation pulse widths are and parasitic capacitance of the device itself becomes an issue at higher modulation frequencies. So although active mode-locking is the most straightforward approach, its maximum frequency is limited to around 40 GHz.

On the other hand if the pulses can modulate the absorption on its own than the net gain window generated by pulse can be as short as the pulse itself. Therefore passively mode-locked lasers can generate shorter pulses than actively mode-locked lasers. The key component in this scheme is an intensity dependent non-linear element called saturable absorber which is responsible for the self-start of mode-locking. The saturable absorber sharpens and narrows the pulses by preferentially passing the high energy peak of the pulses with minimum loss. The pulse shaping process continues until limited by the pulse-broadening mechanisms inside the cavity. Since the pulse shaping is determined by the difference in saturating energies and recovery time constants between the gain and saturable absorber, in case of passive mode-locking it is possible to generate short optical pulses with a repetition rate beyond modulation bandwidths of the semiconductor lasers. However, in the absence of an external reference clock these passively mode-locked lasers suffer from large amplitude and timing jitter instabilities.

Hybrid mode-locking schemes have also been proposed which incorporate active gain modulation along with passive gain modulation from saturable absorber offer the best combination of the above mode-locking techniques. Here the saturable absorption is the dominant mechanism for obtaining short optical pulsewidths while the active modulation stabilizes the pulse stream in amplitude and time. In case of monolithic mode-locked lasers all of these necessary functions of active, passive and hybrid mode-locked lasers can be implemented together on a single semiconductor chip. However, the implementation of

this technique still becomes difficult as the repetition rate increases because of the limitation of the drive electronics.

1.2 Colliding pulse mode-locked lasers

The pulse shaping mechanism can be more effective in case of colliding pulse mode-locking scheme where instead of having a single pulse passing through the saturable absorber at one time we have coherent interaction of two-counter propagating pulses which collide in saturable absorber to generate ultrashort transform limited pulses. The synchronization of the pulses to collide in the saturable absorber occurs because in this case minimum energy is lost to the SA. When the two pulses collide, electric standing waves are formed. The standing-wave intensity is quadruple the intensity of the individual pulses as a result of constructive interference which results in twice as much energy density saturating the absorber than the gain medium. Also the carrier density does not have to be brought to transparency everywhere to allow the pulses to pass with low loss. This enhanced effective saturation cross section of the absorber helps to stabilize and shorten pulses. The two simultaneously counter-propagating pulses also lead to a doubling of the repetition frequency as compared to a conventional mode-locked laser of the same length giving rise to a high repetition rate pulse train without the need for an unpractical shortening of the laser cavity length.

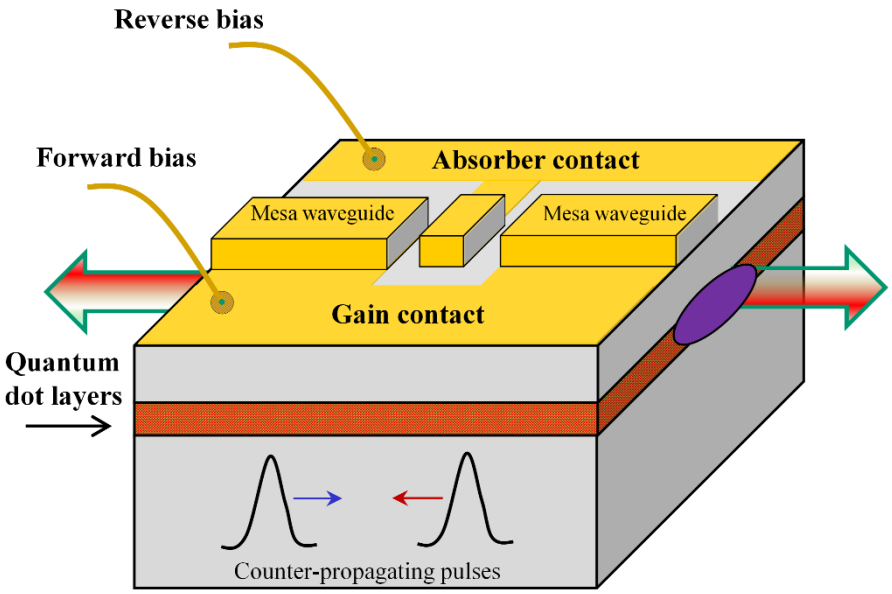

Figure 1: Schematic of a monolithic colliding pulse mode-locked (CPM) laser.

Another interaction in CPM is the formation of transient grating (often referred to as degenerate four-wave mixing) due to the periodic carrier density variation in the saturable absorber region because of the transient standing wave optical field [16], [17]. The carrier generation is high at the peak of the standing wave and low at the standing wave minimum, forming an absorption grating. The grating can reduce the frequency chirp in the mode-locked laser as those portions of the two colliding pulses which collide and have non-equal zero-crossing spacing's under the pulse envelope will not efficiently form the carrier density grating. Thus pulses with frequency chirp encounter higher loss in the saturable absorber compared with unchirped pulses leading to even shorter pulse widths directly from the laser.

However, as in case of any passive mode-locked laser, the spontaneous emission noise produces variations in the timing of each mode-locked pulse and thus increases the

timing jitter. Recent research has been focused towards stabilizing these lasers by either reducing the parasitic capacitance by employing new novel gain materials or by electrical or optical injection locking of these devices [18-20]. Considering the high repetition rates of the monolithic CPM devices, direct modulating at high speeds is still problematic due to the high RC time constants and optical injection locking calls for an external master laser which leads to not so compact system to begin with together with coupling and stability issues arising from having two physically separate lasers. Thus there is a need for a new monolithic scheme which addresses these issues and can be practically implemented in a single optoelectronic integrated circuit.

1.3 Quantum dot based mode-locked lasers

Semiconductor quantum dots, which demonstrate ultrabroad gain bandwidth, ultrafast gain dynamics and easily saturated gain and absorption, have become one of the most promising material systems for the generation of ultrashort pulses. The higher dimensional confinement of QDs as compared to QW leads to an increased ratio of saturation energies in the gain and absorber sections, which is a key parameter in mode-locking. With an extremely broad emission spectrum of more than 100 nm, QD based mode-locked lasers have the potential of generating ultrashort optical pulses. With absorption recovery times as fast as 700 fs already shown, makes this material system an ideal choice for generating high repetition rate optical pulses while the high gain saturation energy facilitates the formation of high peak power pulses. The low threshold current densities, low internal loss, and low confinement factor help to reduce noise. With lower associated spontaneous emission noise as compared to quantum well (QW) devices, the linewidths are generally narrower in QD lasers. The lowest timing jitter values reported so

far in case of mode-locked semiconductor lasers have been in the QD active media, thereby confirming the importance of employing QD materials for future optical communication systems [21]. The same above properties also make the QD material a good choice for ultrafast amplification of these generated optical pulses across a relatively broad spectral range. Ultrafast and distortion free amplification has been already reported at pulse repetition rates of up to 80 GHz, for pulse durations down to 710 fs [22]. With the additional inherent features of being temperature resilient, owing to the absence of higher energy states that can be thermally populated and operation in telecom band of 1260-1360 nm, QD based mode-locked lasers have become suitable candidates for the next generation optical networks.

CHAPTER 2
NOVEL QUANTUM DOT BASED COUPLED-CAVITY COLLIDING PULSE MODE-LOCKED LASER

As mentioned previously, colliding pulse mode-locking in a semiconductor laser is a very effective method for generating optical pulses in the pico to sub-picosecond range. Monolithic CPM lasers are thermally and mechanically stable since there are no moving parts. This together with the added benefits of passive mode-locking, which require no external RF electrical source for pulse generation in principle, makes these lasers an ideal source of highly repetitive optical pulse train without the limitation imposed by drive electronics. However, in the absence of synchronization to an external source these passively mode-locked lasers suffer from large phase noise, which limits there implementation in optical communication systems, where with increasing data capacity more stringent requirements on timing jitter are being imposed.

This chapter outlines a novel QD based coupled cavity laser, where a stable high-Q master laser is used to injection lock a passively mode-locked monolithic colliding pulse slave laser through four-wave mixing in the common saturable absorber. With an all passive stabilization architecture, where both the CPM and high-Q master laser are passively mode-locked, significant reduction in the RF and optical linewidths of the CPM laser is shown. The device design and the fabrication processes involved are also discussed in detail.

2.1 Sub-harmonic optical injection locking

Out of all the injection locking techniques presented recently, sub-harmonic optical injection locking is the most promising to help stabilize a monolithic CPM laser. The technique has obvious advantages over its electrical counterpart as there is no requirement of an external RF source and also does not suffer from the resulting unwanted amplitude modulation (arising from the cavity resonant effect). Stabilization of CPM cavities as short as 174 um (in QW structure) has already been successfully demonstrated using this technique, whereby a stable master laser operating at a sub-harmonic repetition frequency of the slave CPM laser is used to injection lock a passively mode-locked CPM laser [12]. Operation at a sub-harmonic repetition rate of the slave laser has the additional merit of using a low-cost easily available RF source for achieving stable hybrid mode-locking of the master laser. Thus sub-harmonic optical injection locking has proved to be a very effective process by not only being an all optical process by which it does not suffer from electrical bandwidth limitation of semiconductor lasers but also since it does not require the speed and power of electrical drive sources.

2.2 Novel device design concept

With its advantages listed in the last section, sub-harmonic injection locking is a powerful method to stabilize passively mode-locked laser diodes. However, the use of a physically separate master laser still has issues of poor mechanical stability and the requirements of precise optical alignment to achieve pulse injection make it less advantageous in case of optical communication networks where a compact optical source is required. We thus propose a QD based multi-section design where a passively mode-locked monolithic CPM laser is stabilized by injection of optical pulses from a stable high-

Q passively mode-locked ring laser at a sub-harmonic of the cavity resonance frequency in an all-passive stabilization architecture.

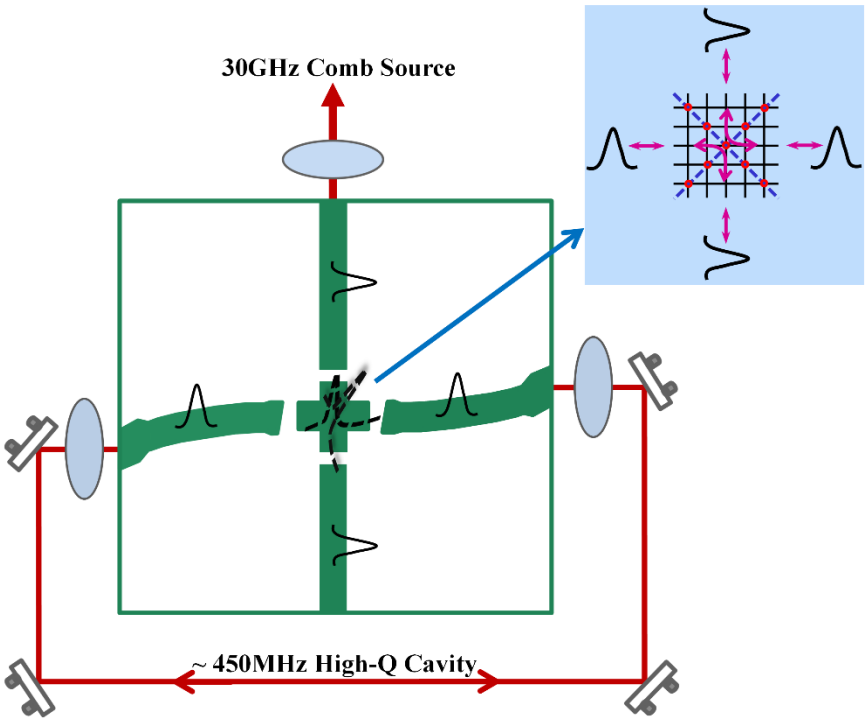

Figure 2: Schematic of the multi-section device. It also illustrates the four-wave mixing process.

As seen in Fig. 2, the two curved gain sections are part of an external ring cavity, which is precisely built and passively mode-locked at a sub-harmonic of the monolithic colliding pulse laser. Having the two cavities in a crossed configuration leads to the formation of transient gratings, when the four pulses overlap in the saturable absorber (SA) region. The formation of the transient gratings (often referred to as degenerate four-wave mixing) is due to the carrier density variation in the SA region. The pulse synchronization happens for the same reason that two counter-propagating pulses meet in the absorber of a

conventional CPM laser. The resulting index of refraction modulation at 45° to the face of saturable absorber causes the pulses to be diffracted from individual cavities into each other, essentially coupling and locking the colliding pulse mode-locked (CPM) laser to the external cavity. This stabilizes and thus effectively reduces the jitter associated with the CPM laser.

2.3 Device design and fabrication

The devices used in this work are fabricated from InAs/InGaAs QD wafer grown by molecular beam epitaxy on a (001) oriented n+ GaAs substrate. As shown in table 1, the active region is a multi-stack QD structure, consisting of 10 layers of self-assembled InAs QDs capped by $In_XGa_{1-x}As$ QWs and bounded by AlGaAs cladding layers. Each QD layer is separated by 33 nm thick GaAs spacers. The devices emit at the telecom wavelength of ~ 1.3 μm.

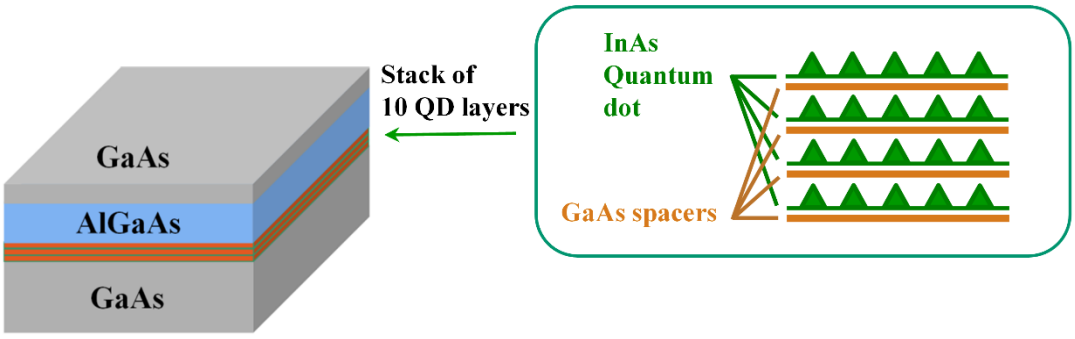

Figure 3: A schematic illustrating the QD wafer structure.

Table 1: InAs/InGaAs quantum dot wafer structure (courtesy Innolume GmbH).

Layer	Material	Group	Repeat	Mole fraction		Thickness	Doping profile		Type	Dopant	n
				start	finish	(nm)	start	finish			1310nm
12	GaAs					200	1e20		P	C	3.411
11	Al(x)Ga(1-x)As			0.35	0	20	3e18		P	C	3.318
10	Al(x)Ga(1-x)As			0.35		1000	1e18		P	C	3.225
9	Al(x)Ga(1-x)As			0.35		500	5e17		P	C	3.225
8	GaAs	1	10			33			U/D	None	3.411
7	In(x)Ga(1-x)As	1	10	0.15		5			U/D	None	3.5
6	InAs	1	10			0.8			U/D	None	3.5
5	GaAs					33			U/D	None	3.411
4	Al(x)Ga(1-x)As			0.35		500	5e17		N	Si	3.225
3	Al(x)Ga(1-x)As			0.35		1000	1e18		N	Si	3.225
2	Al(x)Ga(1-x)As			0	0.35	20	3e18		N	Si	3.318
1	GaAs					500	3e18		N	Si	3.411
0	GaAs substrate				N+ GaAs 3 inch						3.411

The fabricated monolithic device structure is shown in Fig. 4. It consists of four gain sections with two crossed SA's at the symmetry center in order to maximize the coherent coupling of the four colliding pulses. Mesa structures are defined using standard ridge waveguide laser processing. The sample is wet-etched to form 3.6 and 4.6 μm wide single mode waveguides in the case of curved and linear sections, respectively. The curved section waveguides are designed at an angle of 7° with respect to the facet and are tapered to 4.6 μm widths at the termination. The waveguides are angled and tapered to avoid Fabry-Perot (FP) reflections [23]. The effective modal reflectivity is given by

$$R = R_0 e^{-(\frac{\pi n W \theta}{\lambda})^2}$$

where, R_0 is the Fresnel reflectance, n is the effective refractive index of the waveguide, W is the mode width, θ is the angle from the normal to the facet, and λ is the wavelength. As can be seen the modal reflectivity can be reduced by increasing the waveguide angle and the modal width. The increase in modal width is achieved by tapering the waveguides near the facets. The SA sections are 4.6 μm wide and 200 μm long waveguides, separated

by a 15 μm gap from the gain sections. All the gain and SA sections facets are further angled relative to each other to avoid FP reflections. Benzocyclobutene (BCB) polymer is used for planarization and standard Ti-Au and Ni-Ge-Au metal contacts are used for the p and n-side of the wafer after lapping and polishing. All four gain sections are electrically isolated from each other, allowing for individual control of the DC bias currents to help achieve optimal mode-locking. No anti-reflection (AR) coatings are used on the cleaved facets (R ~ 32%). Single mode operation is verified with effective index method and beam profiling and by efficient coupling to single mode fiber (SMF).

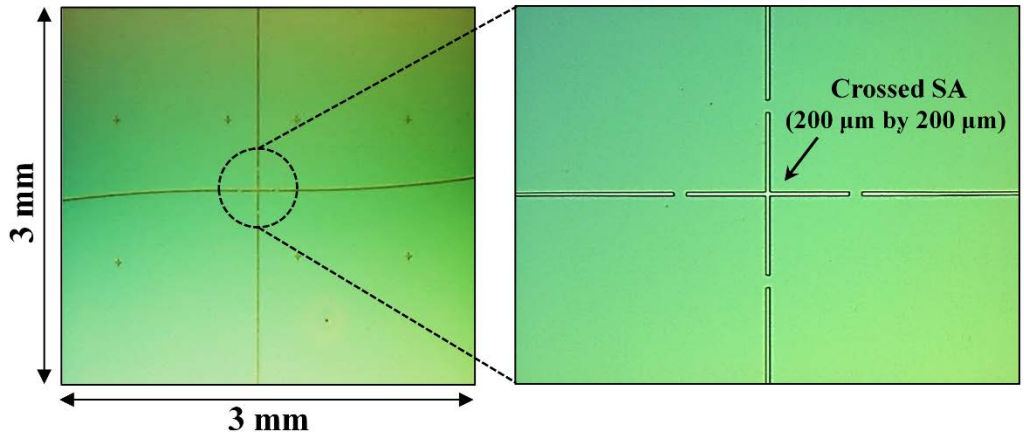

Figure 4: (Left): Fabricated device before metallization with BCB as the isolation layer (seen in green). (Right): Magnified picture showing crossed saturable absorbers, each being 200 μm in length.

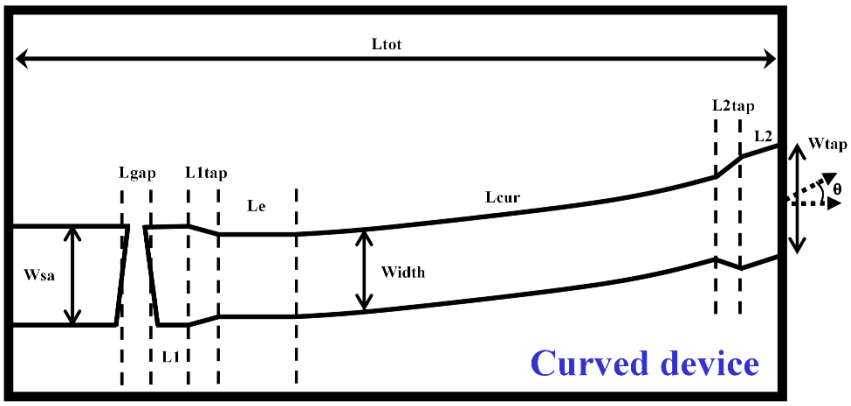

Figure 5: Photomask parameters of the curved two-section device.

Table 2: Photomask parameters for the curved and saturable absorber sections in the multi-section device.

	L_{tot}	L_{sa}	W_{sa}	L_{ga}	L_1	L_{1ta}	W_g	L_e	θ	L_{2ta}	L_2	W_{ta}
[μ	15	20	5	15	30	80	4	0	7°	70	30	5

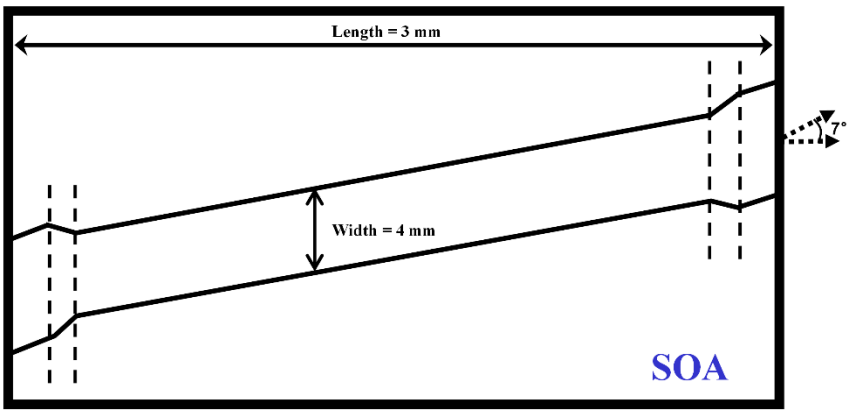

Figure 6: Photomask parameters of the semiconductor optical amplifier (SOA) device.

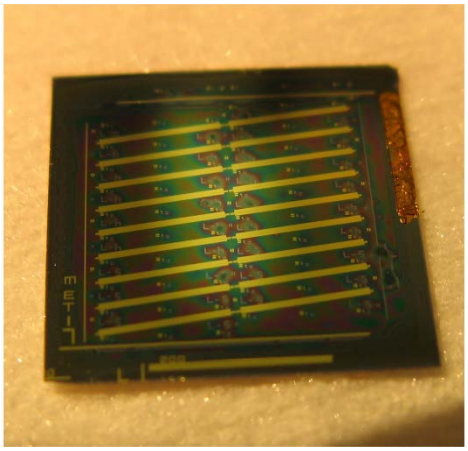

Figure 7: Bars of (two not cleaved bars consisting of nine devices each) fabricated SOAs before cleaving.

The semiconductor optical amplifiers (SOA) used to amplify the output of the lasers are fabricated using the same QD wafer and consist of 4 μm wide and 3 mm long ridge waveguide angled at 7° to the facet. The nominal small signal gain of these devices with and without AR coatings is around 21 dB and 13 dB respectively. The multi-section device and the SOA's are mounted p-side up on a copper heat sink and are maintained at a constant temperature (20° C) using a thermoelectric cooler.

2.3.1 Fabrication procedure

1. QD wafer cleaving and degreasing

- The wafer is cleaved along the appropriate crystalline axis
- And subsequently cleaned with acetone, methanol and iso-propanol
- If required the sample is briefly immersed in an ultrasonic bath at low power

2. Photolithography

- Spin coat S1805 positive resist
  - 3500 rpm for 40 sec
  - 500 nm thickness
- Pre-bake (120°C for 4 min)
- UV exposure (12mW for 5.5 sec)
- Develop in 351:DI (10ml:70ml for 35 sec)
- Post-bake (120°C for 4 min)

Note: The waveguide is located along major axis [011]. The wet etchant used results in mesa ridge waveguide structure regardless of the wafer orientation.

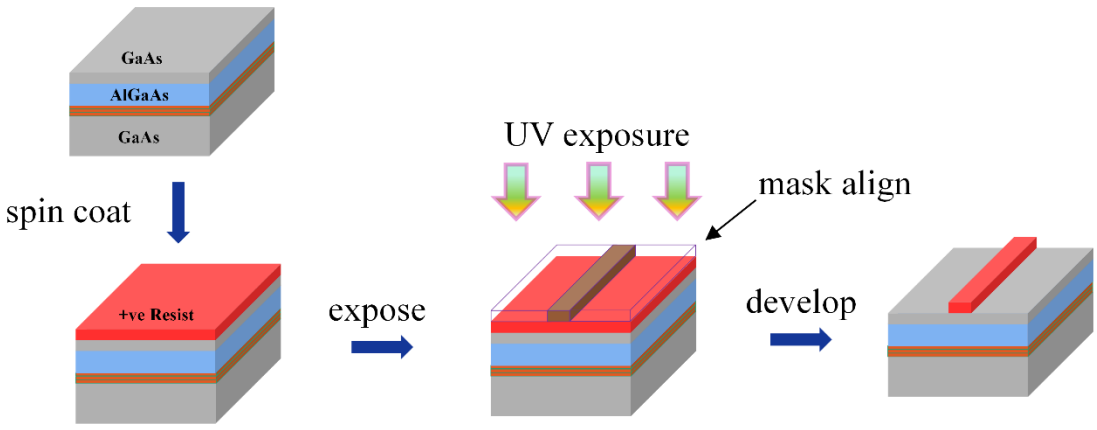

Figure 8: Schematic illustrating positive photolithography steps.

3. Wet-etching and resist removal

- Etchant used H_3PO_4:H2O2:DI (5ml:10ml:250ml for 8 min)
  - Etching ratio is around 160 nm/min
  - Etching depth is around 1.4 to 1.5 μm
- Resist removal using acetone

Note: No stop layer

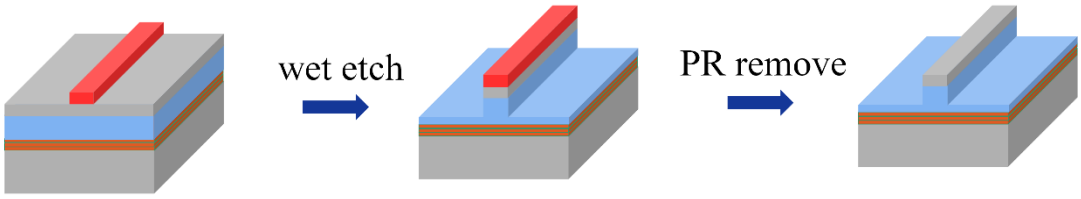

Figure 9: Mesa ridge-waveguides are formed in a single wet-etching step.

4. Benzocyclobutene (BCB) coating, curing and etching

BCB polymer is used as the insulation layer in our devices. BCB is a low-dielectric constant polymer developed by Dow Chemical Co. to replace silica as dielectric for on-chip interconnects and microelectronic packaging. It's the dielectric material of choice for many applications in the electronic industry because of its **low dielectric constant**, a **low electrical current loss factor (i.e. low dielectric loss) at high frequencies**, low moisture absorption, low cure temperature, high degree of planarization, low level of ionic contaminants, high optical clarity, good thermal stability, excellent chemical resistance, and good compatibility with various metallization systems.

- Spin coat Adhesion Promoter AP3000 (4000 rpm for 40 sec)
- Spin coat BCB (4000 rpm for 40 sec)
- Hard cure BCB (in N_2 ambient atmosphere)

Table 3: Hardcure temperature profile.

Step 1	5 min. ramp to 50°C	5 min. soak
Step 2	15 min. ramp to 100°C	15 min. soak
Step 3	15 min. ramp to 150°C	15 min. soak
Step 4	60 min. ramp to 250°C	60 min. soak
Step 5	natural cool down	

- Dry-etch BCB using RIE
  - O2:CF4 (10ccm:5ccm for ~ 9 min)
  - Etching ratio is 150nm/min
- Soak in Ash Residue Remover (ReziTM-28 for 5 min)

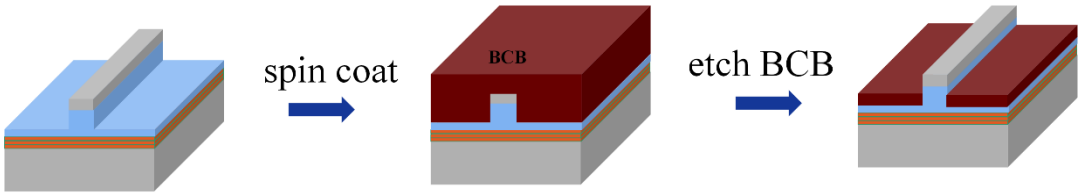

Figure 10: BCB polymer is used as the dielectric insulation layer.

5. Photolithography

- Spin coat NR7-1000PY negative resist (4000 rpm for 40 sec)
- Pre-bake (150°C for 4 min)
- UV exposure (12mW for 14 sec)
- Develop in 351:DI (10ml:70ml for 35 sec)
- Post-bake (150°C for 4 min)

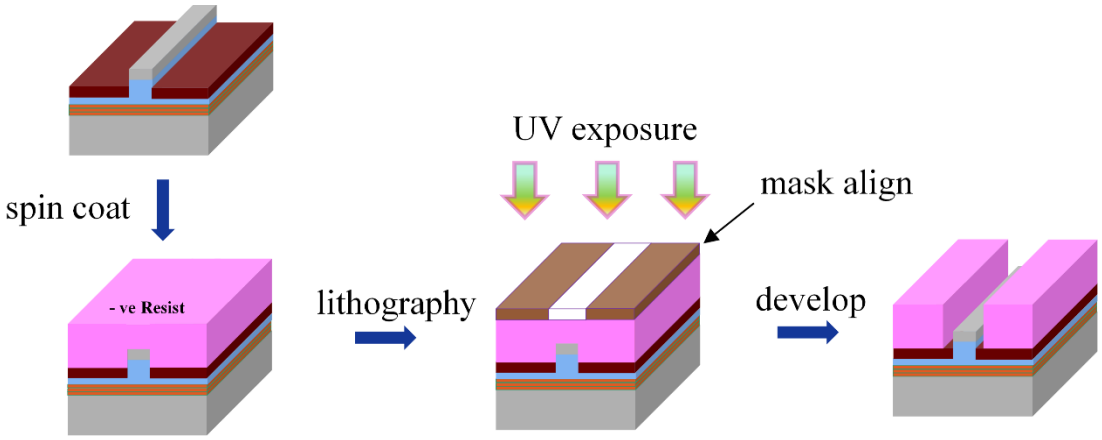

Figure 11: Schematic illustrating negative photolithography steps for depositing p-side metal contacts.

6. P-side metallization

Ohmic contact is created using Ti and Au followed by high-temperature anneal in a protective N_2 gas ambience.

- De-oxidation using H_3PO_4:DI (6ml:180ml for 5 sec)
- Metal deposition, Ti (5nm) and Au (300 nm)
- Lift-off using Resist Remover (RR2 for 5 min)
- Rapid thermal annealing (RTA = 400°C for 1 min)

Note: It's a non-alloy ohmic contact (because of high doping density of Carbon in p-GaAs ~ 10^{20}) where Ti is used as an adhesive layer to promote adhesion of Au to GaAs. High-temperature annealing improves the contact resistivity (resistivity < 10^{-6} Ωcm^2).

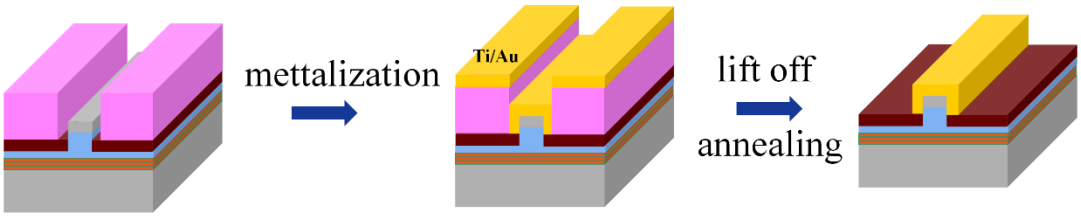

Figure 12: P-side metallization is followed by annealing at 400°C.

7. Lapping and polishing

Lapping is used to reduce the wafer thickness. This helps when cleaving individual devices from the bar later. The lapped surface is subsequently prepared for n-side metallization by polishing it to a mirror finish.

- Lapping using Al_2O_3 powder (5 µm size) to reduce the wafer thickness to around 150 µm.
- Polishing using Al_2O_3 powder (0.3 µm size)

Note: Rough polishing (instead of mirror finish) can be used to prevent substrate modes caused by reflection from the bottom n-side metal contact.

Figure 13: The wafer is lapped and polished to a thickness of ~ 150 µm before cleaving into individual devices from the device bar.

8. N-side metallization, cleaving and mounting

Ohmic contacts are metalized onto the waveguides by thin-film evaporation whereby, Ni, Ge and Au are deposited using thermal evaporation and the metal film is then heated (in a protective N_2 gas ambience) to the eutectic temperature to alloy the ohmic metal to the semiconductor.

- De-oxidation using H_3PO_4:DI (6ml:180ml for 5 sec)
- Metal deposition, Ni (2nm), Ge (20nm) and Au (200 nm)
- Rapid thermal annealing (RTA = 400°C for 1 min)

Note: It's an alloyed ohmic contact (resistivity better than 10^{-6} Ωcm^2 shown) where Ge serves as the dopant. Ni has the role of avoiding the balling up of Au-Ge alloy, reduce the formation of surface oxides and to facilitate the incorporation of Ge dopant.

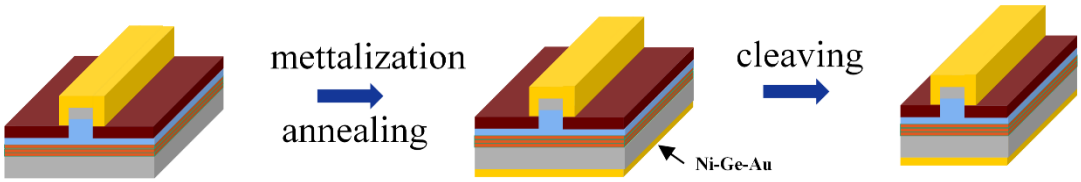

Figure 14: After n-side metallization and annealing at 400°C, individual devices are cleaved and mounted on gold-coated copper studs.

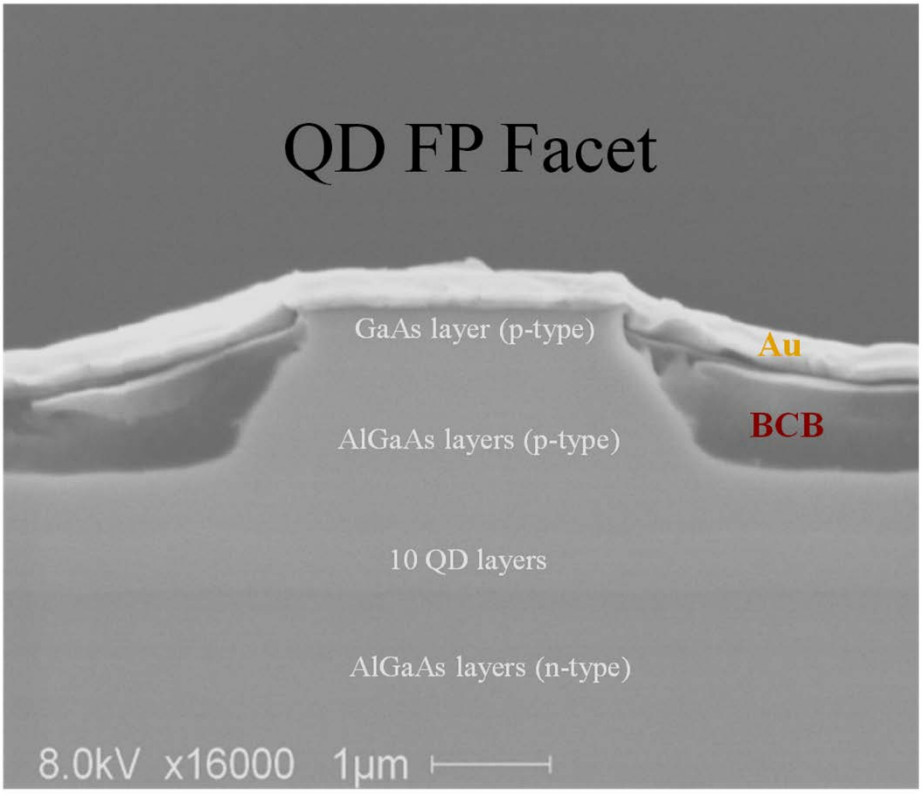

Figure 15: SEM image of the facet of a fabricated device.

The individual devices are precisely cleaved using a diamond tip mounted on a three axis translation stage and subsequently soldered on a gold coated copper stud. Au bonding wire is used to make electrical connections to the cleaved device since Au wire bonded to Au bonding pad is extremely reliable as the bond is not subjected to interface corrosion or intermetallic formation.

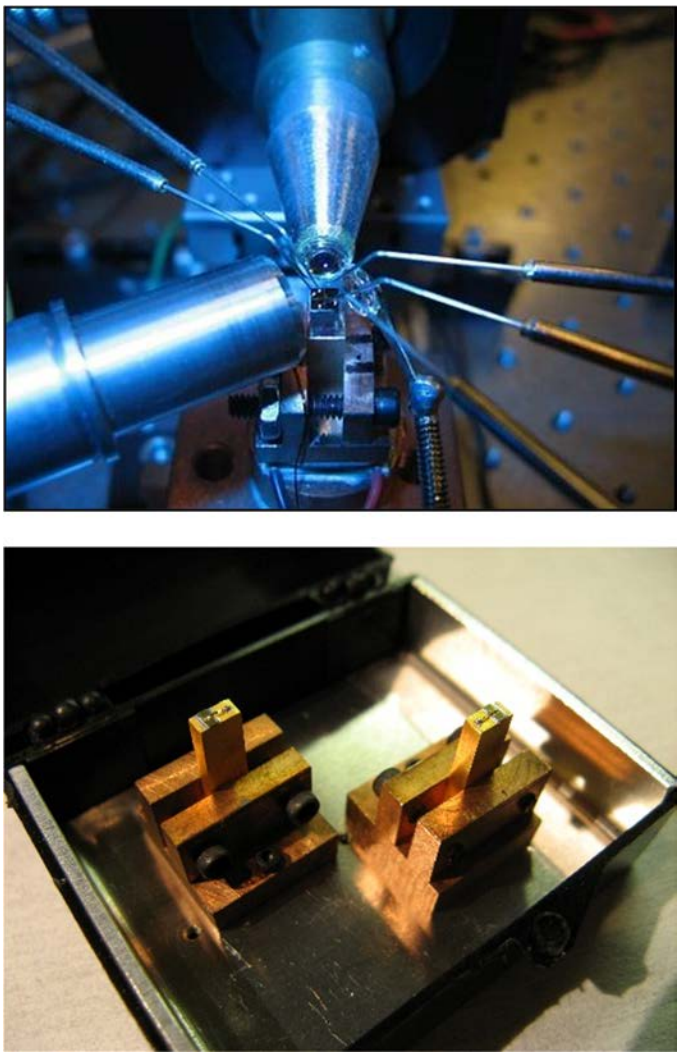

Figure 16: Multi-section device mounted inside the setup. Shown below are SOAs mounted on gold coated copper studs.

2.3.2 Broadband anti-reflection coatings

Anti-reflection coatings are used on the fabricated quantum dot amplifiers to reduce the facet reflectivity and improve the overall power output from these devices. The coatings are fabricated in-house using an e-beam evaporator with an in-situ ellipsometer. The real time in-situ ellipsometric monitoring is useful for control of the coating process and offers better accuracy and reliability than crystal monitors, especially for sub 100 nm optical

thickness. Considering the broad gain bandwidth (>100nm) of the quantum dot SOA's a three layer W-coat design is used. The three layer structure achromatizes the design over a broad bandwidth. The three materials used in our coating are Al_2O_3, Si and SiO_2 and the optical thicknesses used are optimized over the highest bandwidth possible (with low reflectivity) using "Essential Macleod" thin film software.

Table 4: Anti-reflection coating parameters (reference wavelength $\lambda = 1310$ nm).

Layer	n	t (nm)
Air	1.000	
SiO2	1.438	241
Si	3.507	34
Al2O3	1.800	48
Substrate	3.408	

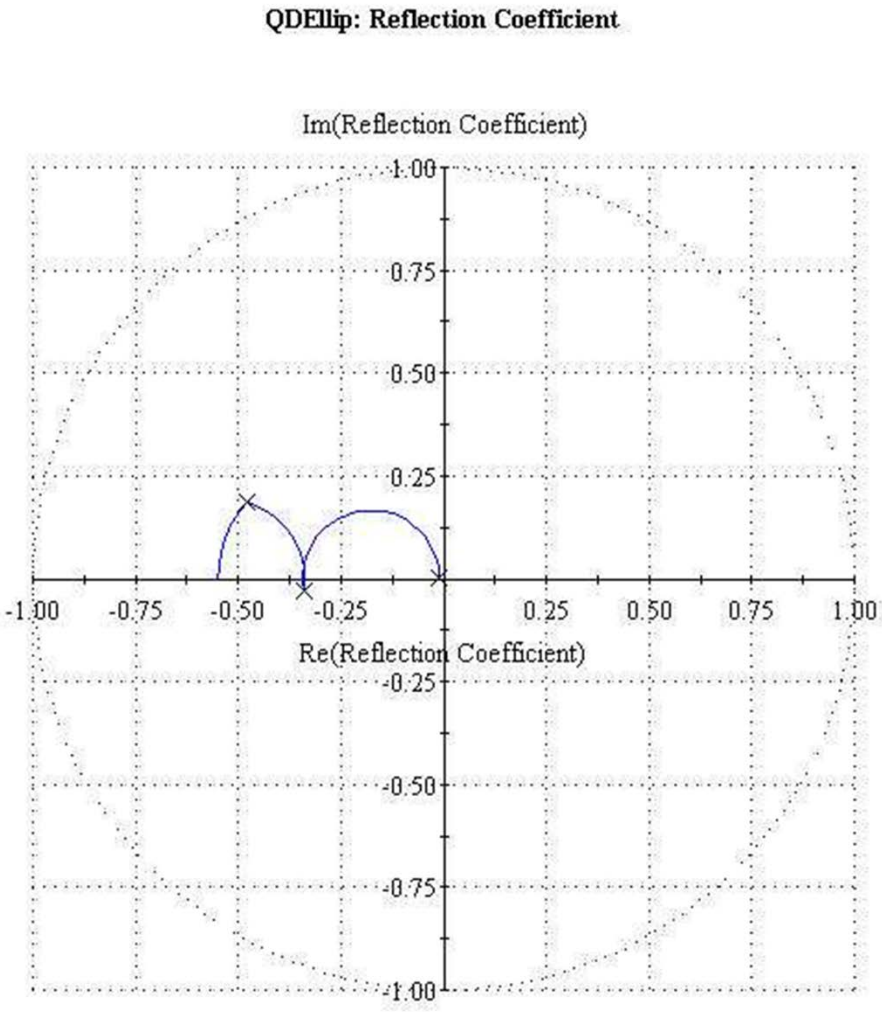

Figure 17: Reflectance diagram (for s-polarization).

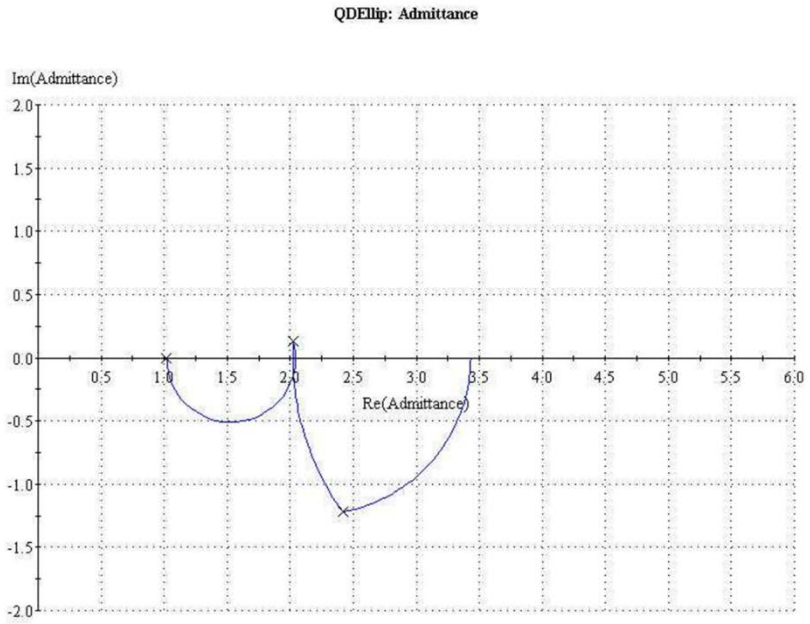

Figure 18: Admittance diagram (for s-polarization).

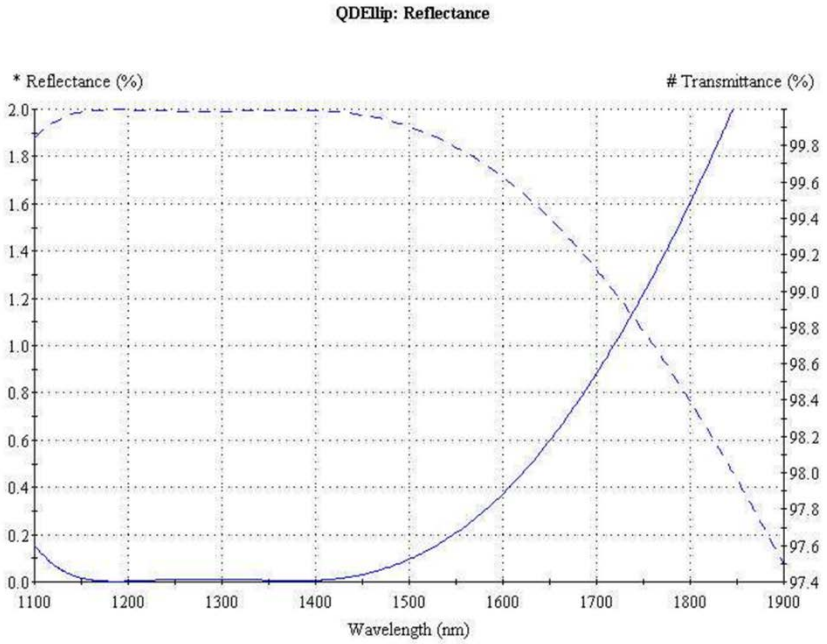

Figure 19: Calculated reflectance and transmittance (for s-polarization) of the 3-layer coating. Reflectance is shown using bold line.

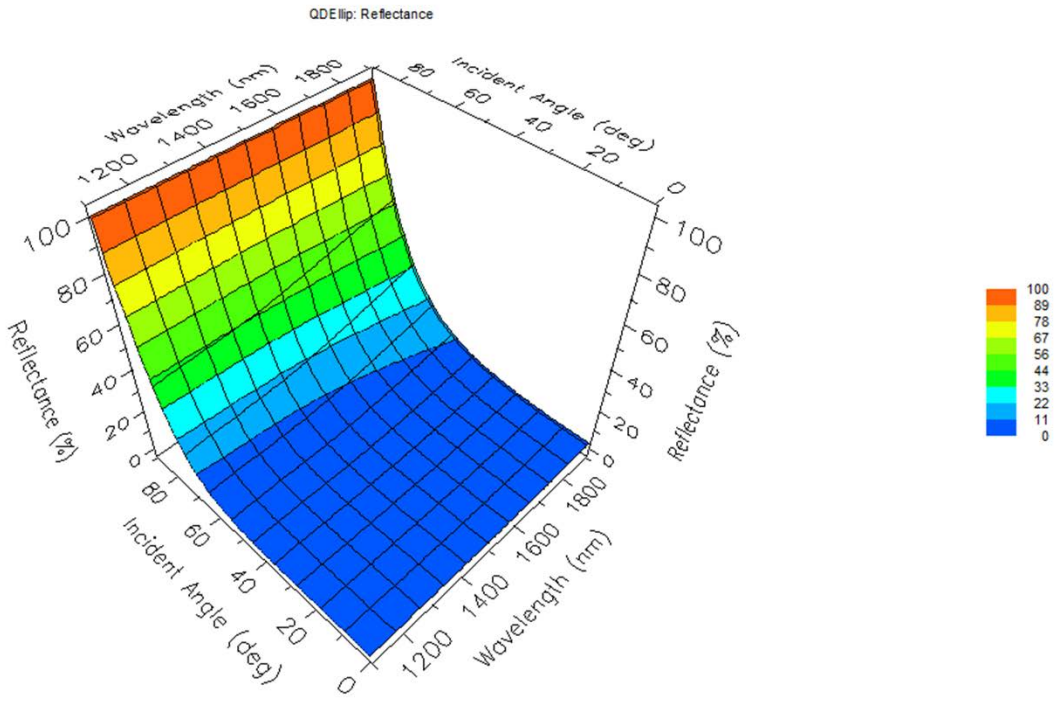

Figure 20: Calculated reflectance as a function of incident angle.

Initial measurements of the reflectivity of the three layer coating was done by coating a linear 1.5 mm long monolithic fabry-perot quantum dot laser (λ_c = 1270 nm) with cleaved facets (R~30%). Kaminow-Eisenstein method, which is based on Hakki-Paoli, is used for the determination of the reflectivity of the coated device [24]. The device is mounted and operated just below threshold current and the modulation of intensity measured using an optical spectrum analyzer. The depth of modulation is given by

$$m = \frac{P_{\max} - P_{\min}}{P_{\max} + P_{\min}} \text{ , with } m = \frac{2|a|}{1+|a|^2} ; \quad R_L^* = a^2 R_L$$

Here “a” is the amplification factor. The reflectivity R_L^* of the coated facet is then calculated using the known cleaved facet reflectivity $R_L = 0.3$. The measured modulation intensity and the calculated reflectance for the fabry-perot device are shown in Fig. 22. As seen, even at high pumping currents no lasing is observed. The coatings when fabricated on the 3 mm long quantum dot amplifiers resulted in an improvement in the resultant gain from these devices which improved from ~ 12 dB to more than 19 dB (with SOA biased at I = 300 mA).

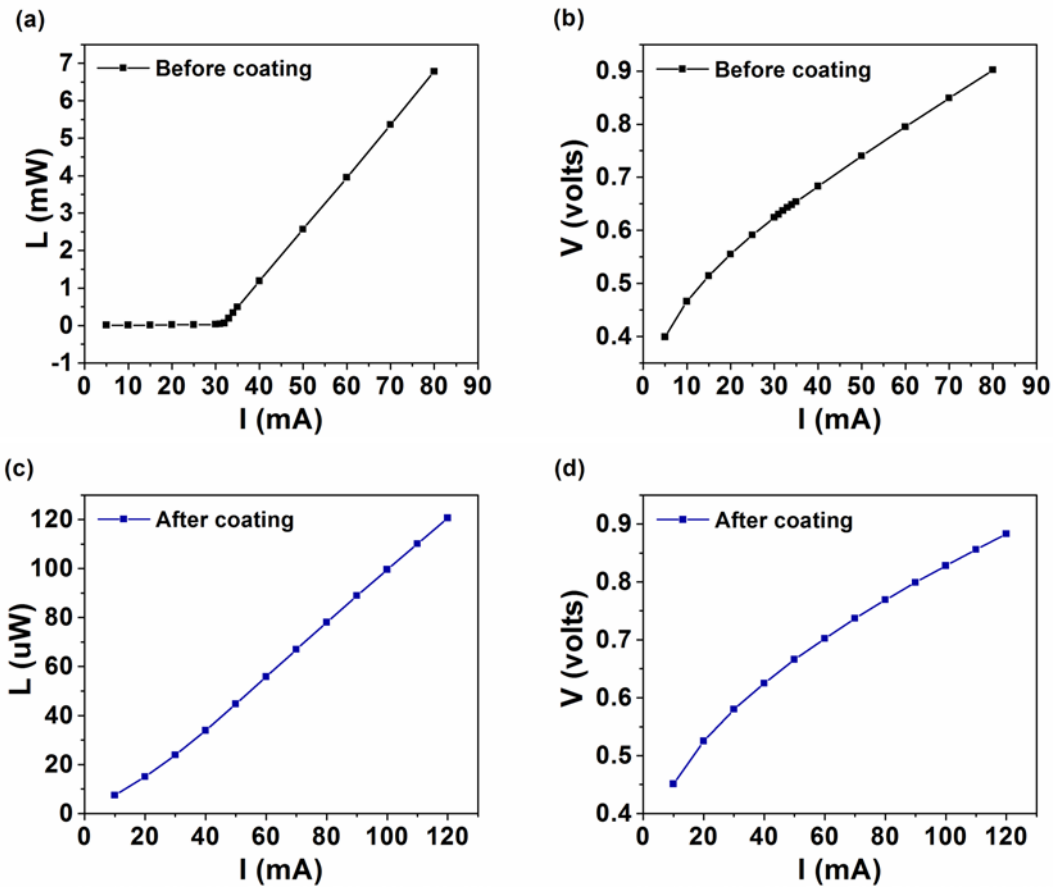

Figure 21: LI-IV curves of the 1.5 mm Fabry-perot laser before and after AR coating.

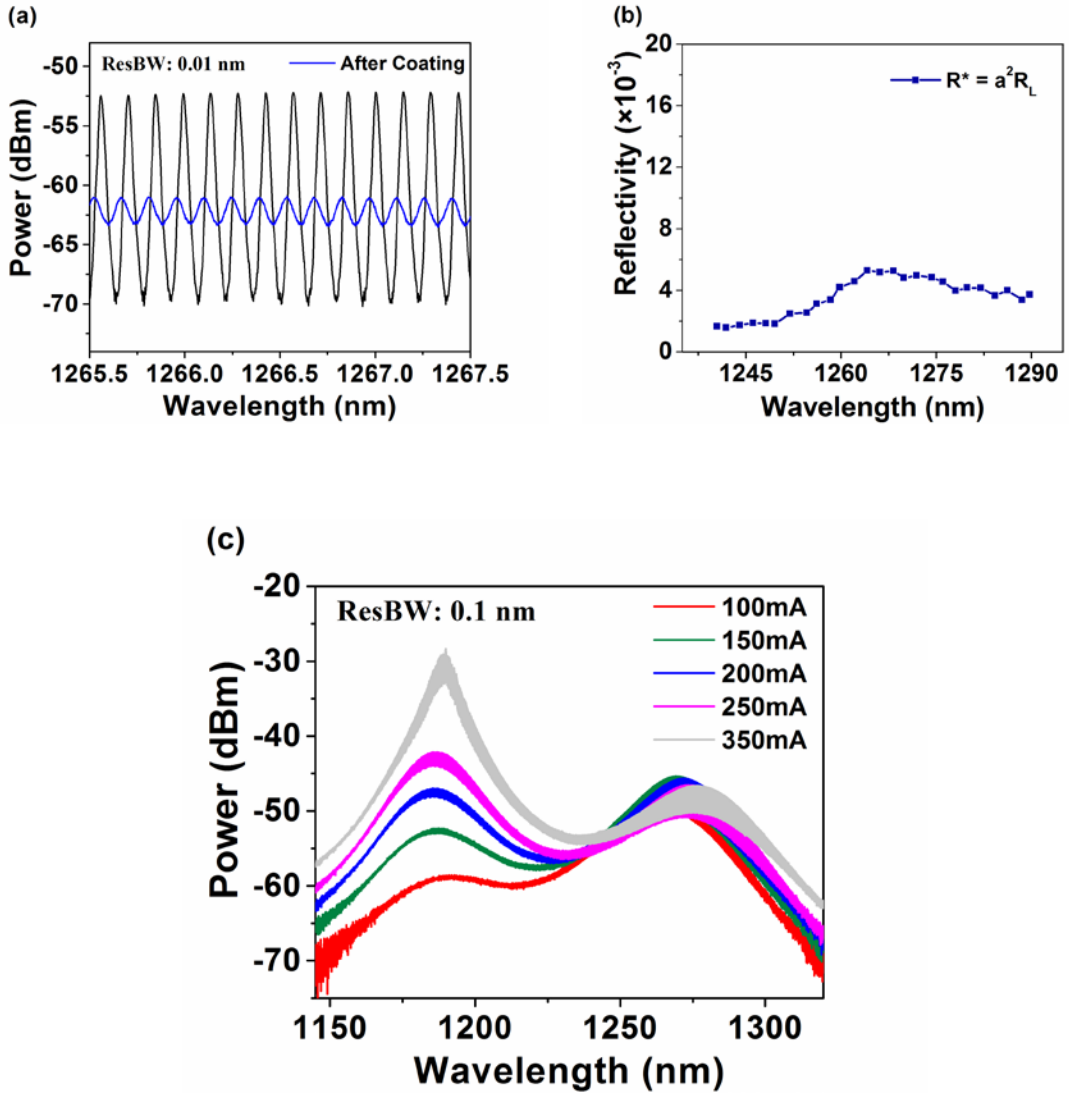

Figure 22: Measured reflectivity of the coated fabry-perot laser (λ_c = 1270 nm) using Kaminow-Eisenstein method. Also shown is the optical spectrum with no lasing seen even at higher injection currents.

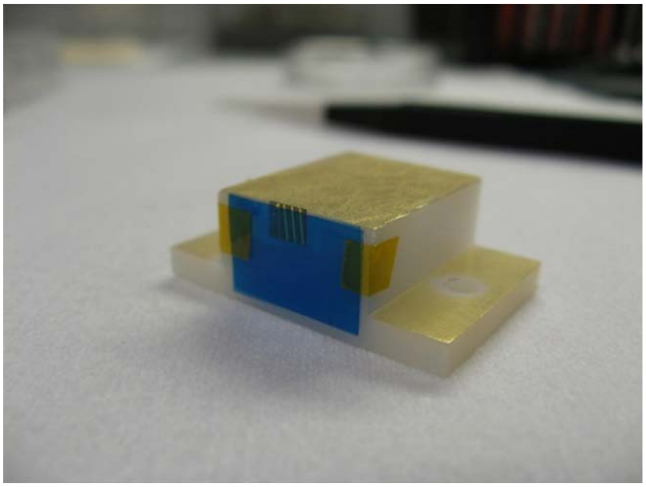

Figure 23: Delrim fixture with a bar of SOAs for AR coating

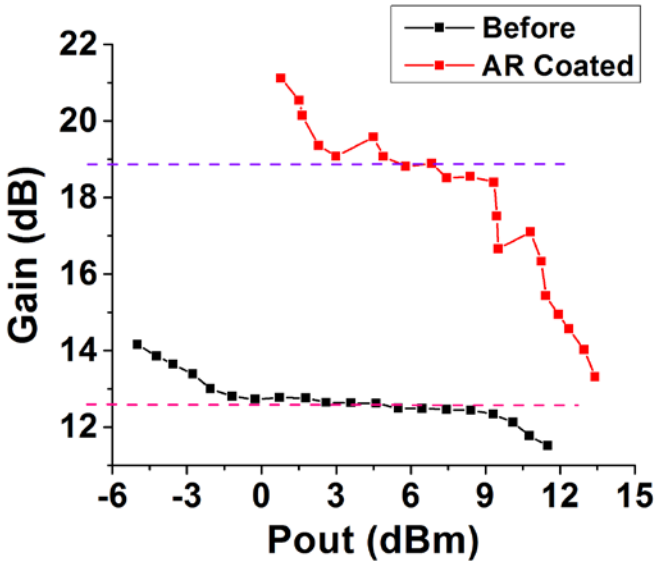

Figure 24: Graph showing the gain comparison of the coated and uncoated SOAs.

2.4 Experimental setup

Fig. 25 illustrates the experimental setup. The monolithic CPM cavity formed by the cleaved facets has a total length of about 2.8 mm. However because of the two counter propagating pulses traveling simultaneously in the cavity, the fundamental repetition rate in the CPM configuration is twice the free spectral range of the whole cavity. The CPM resonant cavity thus has a repetition rate of 29.46 GHz. For the master oscillator, the two curved sections serve as the gain medium. As seen in the figure, the cavity is built with four gold coated external mirrors, with two mirrors mounted on a translation stage to control and precisely match the cavity length to a sub-harmonic of the CPM laser. The chosen cavity length corresponds to a free spectral range (FSR) of 446 MHz which is the 66^{th} sub-harmonic of the CPM laser. In the operation mode, all the gain sections are driven by constant-current sources, while a voltage source provides the reverse bias to the absorber sections.

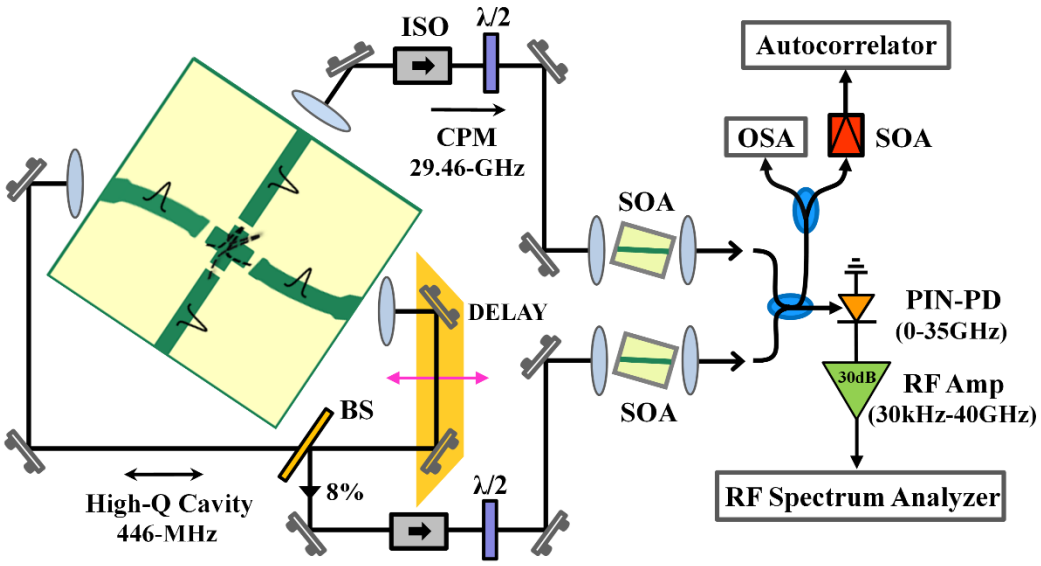

Figure 25: Schematic drawing of the experimental setup. SOA, semiconductor optical amplifier; BS, pellicle beam splitter (92-8%); λ/2, half-wave plate; ISO, optical isolator; OSA, optical spectrum analyzer.

It should be noted that because of the common SA region, the reverse bias voltage and the bias currents used in the experiment are carefully chosen to achieve simultaneous stable mode-locking of the external cavity and the CPM laser and to achieve optical spectral overlap of the two cavities. The spectral overlap induces coupling between the two cavities whereby the injected pulses transfer the phase stability to the longitudinal modes of the CPM slave laser, thus injection locking the CPM laser to the master laser.

2.5 Measurement and results

To begin, the external ring cavity is first aligned to operate in a continuous wave (CW) regime by applying forward bias current of 70 mA on each of the two curved gain sections, using separate DC probes and current sources. The threshold current of the laser is ~ 35 mA (applied on each gain section with no voltage on the absorber section). Two aspheric lenses are used to collect and collimate the light inside the ring cavity. Passive mode-locking is achieved by applying reverse bias voltage of -6.5 V to the crossed SA section, which is kept constant through all measurements. The light is coupled out of the ring cavity using a pellicle beamsplitter with small reflectance (8%) to minimize the cavity losses. The output is amplified using an SOA and then coupled to single mode fiber for diagnostics. A free space optical isolator is used to avoid coupling of the SOA emission back into the master oscillator and a half-wave plate serves to match the TE polarization of the SOA. The spectral and autocorrelation measurements are shown in Fig. 26. The 3 dB spectral width is 3.6 nm. The pulse width is estimated to be 5.21 ps, assuming a Gaussian pulse shape. The time-bandwidth product (TBP) is thus 3.29, which is 7.5 times transform limit.

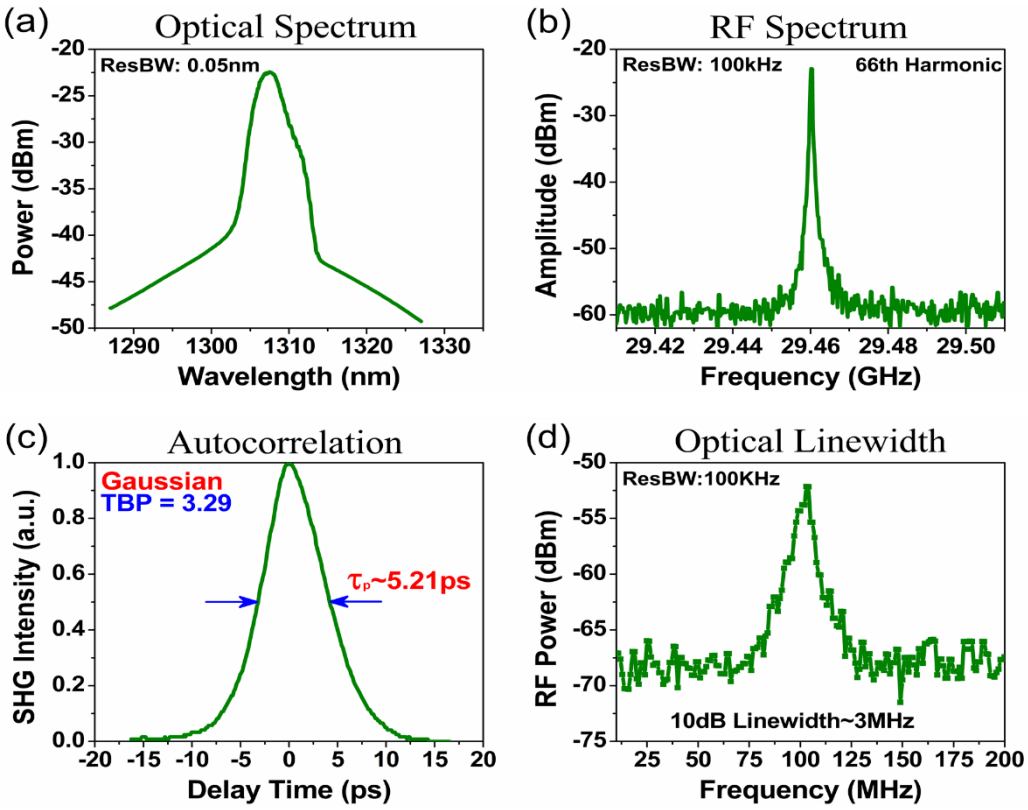

Figure 26: Spectra of the passively mode-locked high-Q external cavity (master) laser: (a) Optical spectrum, (b) RF power spectrum showing 66th harmonic, (c) Autocorrelation trace, (d) Optical linewidth, measured using the self-heterodyne setup.

The optical linewidth in Fig. 26 (d), is measured using the delayed self-heterodyne technique [25]. The schematic of the setup is shown in Fig. 27. The laser output is amplified using a fiberized amplifier before the Mach-Zehnder interferometer. A free space acousto-optic modulator operating at 100 MHz in one of the arms together with 200 meters fiber delay in the other produces an uncorrelated beat tone at 100 MHz on the electrical spectrum analyzer which gives us the measure of the average optical linewidth, as it's the result of a heterodyne beat of two combs. Derickson outlines a comprehensive method for

determining the linewidth of a laser following Lorentzian linewidth statistics [25]. Since semiconductor laser linewidths are dominated by frequency jitter, or 1/f noise, linewidths are measured more accurately by determining the width at levels further down from the peak than the half-maximum. Since a delayed self-heterodyne beat result in a convolution of Lorentzian curves, a deconvolution factor is necessary. For the 10 dB width, this factor is $2\sqrt{9}\,\Delta\nu$. The measured 10 dB average optical linewidth of the master laser is ~ 18 MHz which thus yields a laser linewidth of $\Delta\nu = 3$ MHz, after deconvolution.

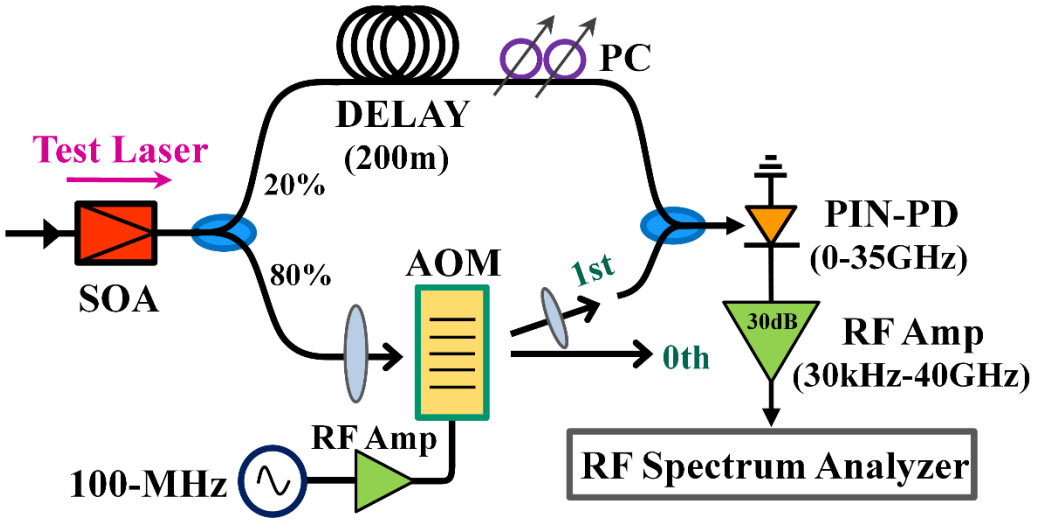

Figure 27: Schematic drawing of the delayed self-heterodyne setup used to measure the optical linewidth of both lasers. SOA, semiconductor optical amplifier; AOM, acousto-optic modulator; PC, polarization controller; PD, photodetector.

The slave CPM laser is passively mode-locked at the fundamental repetition rate of 29.46 GHz by applying a forward bias current of 28 mA on each of its linear gain sections. The reverse bias voltage is -6.5 V which, as mentioned, is shared and kept constant with the SA of the master oscillator. The threshold current of the laser is ~ 20 mA (applied on each gain section with no voltage on the absorber section). Light is coupled out using an aspheric lens and then amplified using an SOA before going to the diagnostic equipment. As seen in Fig. 28(a), the laser exhibits supermode noise (a characteristic of harmonic mode-locking) with the optical spectrum showing two sets of optical modes spaced at the cavity FSR. The measurements before injection are taken by physically blocking the light inside the master ring cavity. Optical pulse injection is achieved by removing this beam block. As seen in Fig. 28, supermode suppression in the optical domain is not only accompanied by RF linewidth reduction but also by reduction in the average optical linewidth after injection locking. There is a more than 10 dB reduction in the RF noise level at 20 MHz offset from the carrier. The RF tone width is reduced from 24.35 MHz to 4.88 MHz measured 30 dB down from the carrier, which is an almost 5-times reduction. This is accompanied by a reduction of the 10 dB average optical linewidth, from 46 MHz to 18 MHz. After deconvolution, this corresponds to a laser linewidth reduction from ~ 8 MHz to 3 MHz after injection locking. The intensity autocorrelation measurements are shown in Fig. 28 (d). The pulse width is estimated to be 4.32 ps, assuming a Gaussian pulse shape. The 3 dB spectral width is 1 nm. The TBP is thus 0.757, which is 1.72 times transform limit. The autocorrelation trace (and hence the pulse width) remains unaffected by injection locking.

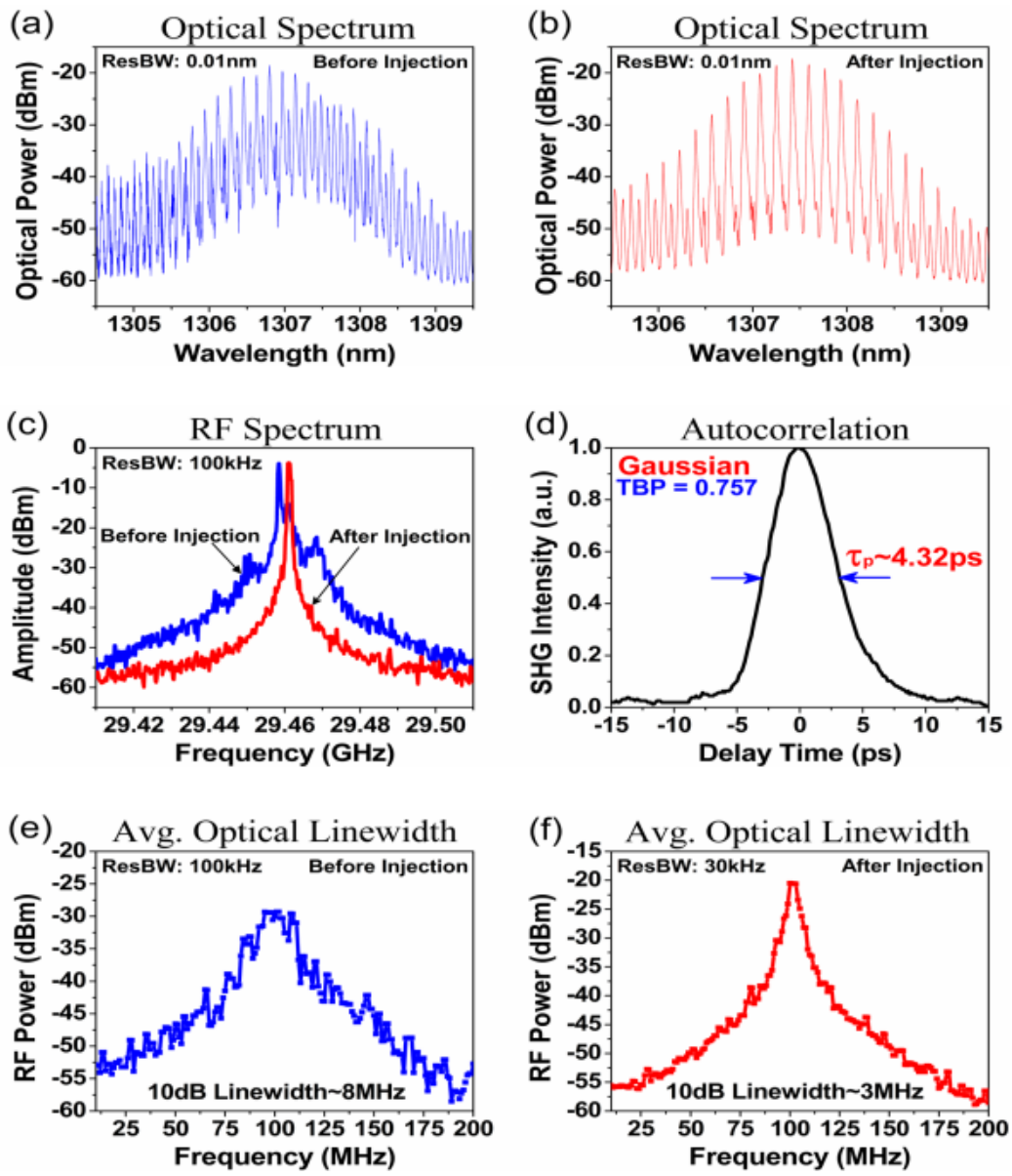

Figure 28: Spectra of the passively mode-locked CPM (slave) laser before (in blue) and after (in red) optical injection: (a) Optical spectrum before injection, (b) Optical spectrum after injection, (c) Comparison of RF power spectrum showing almost 5-times reduction in the 30 dB RF linewidth after injection, (d) Autocorrelation trace, remains indistinguishable after injection locking (e) Optical linewidth before injection, (f) Optical linewidth after injection showing close to 3-times reduction in the 10 dB optical linewidth.

The mechanism of stabilization can be explained as due to the optical pulse injection from the master laser into the CPM cavity, which injection locks the CPM laser to the stable master oscillator. Injection locking is confirmed by the supermode suppression and the reduction in the optical linewidth of the CPM laser, which is seen to closely match the linewidth of the master. The adjustment of the optical pulse timing of the CPM laser by the pulses of the master oscillator further leads to the sharpening in the RF spectrum peak and hence the RF linewidth reduction. However, the pulse width of the CPM laser remains the same after injection locking, indicating that the main pulse-formation mechanisms such as saturable absorption and saturable amplification are still dominated by the slave laser. Because the four pulse interaction is only occurring periodically (every 66^{th} pulse of the slave laser), pulse shortening does not occur as might be expected with higher optical intensity in the SA. As mentioned earlier, the injection locking occurs because of the transient grating formation at 45° to the face of the SA which is responsible for the interaction between cavities. Since the diffraction efficiency from the transient gratings induced by the pulse overlap is estimated to be ~ 10^{-3}, which is orders of magnitude larger than any other linear scattering effect such as diffractive signal leakage, this indicates that the injection locking mechanism is predominantly due to four-wave mixing.

CHAPTER 3
CONFIRM FOUR-WAVE MIXING PROCESS AS THE PRIMARY INJECTION LOCKING MECHANISM

In this chapter we describe an experiment to confirm FWM process as the primary mechanism responsible for the observed injection locking in the novel design. This is the first time, to the best of our knowledge that FWM has been conclusively shown to be used for injection locking in semiconductor media especially in an orthogonal waveguide configuration. We also subsequently investigate the contributions from other mechanisms such as linear scattering which are found to be negligible as expected in the case of low-index contrast perpendicular waveguide crossings [26], [27].

3.1 Experimental setup

Fig. 29 illustrates the experimental schematic. Under normal operating conditions, both lasers operate bidirectionally i.e., both lasers are operating in the CPM regime. However, in order for the FWM effect to be unambiguously identified, a free space circulator is added to force unidirectional operation of the ring laser and allow access to the ASE output in backwards direction from the other facet (port-2) of the ring laser. This counter-clockwise ASE output is analyzed before and after injection to confirm the FWM process.

The devices used in the experiment are the same as described previously. The monolithic CPM cavity is cleaved at a length of 2.8 mm and is passively mode-locked by applying a negative bias voltage to the SA section. With a forward bias current of ~ 25 mA on each of the linear gain section and a reverse bias voltage of -6.1 V ± 0.1 V on the SA, the laser typically emits close to transform limited pulses of some few picoseconds. It should be noted that because of two counter-propagating pulses traveling simultaneously in the cavity, the repetition rate in the CPM configuration is twice the free spectral range (FSR) of the whole cavity. The monolithic CPM cavity thus has a pulse repetition rate of ~ 29.44 GHz.

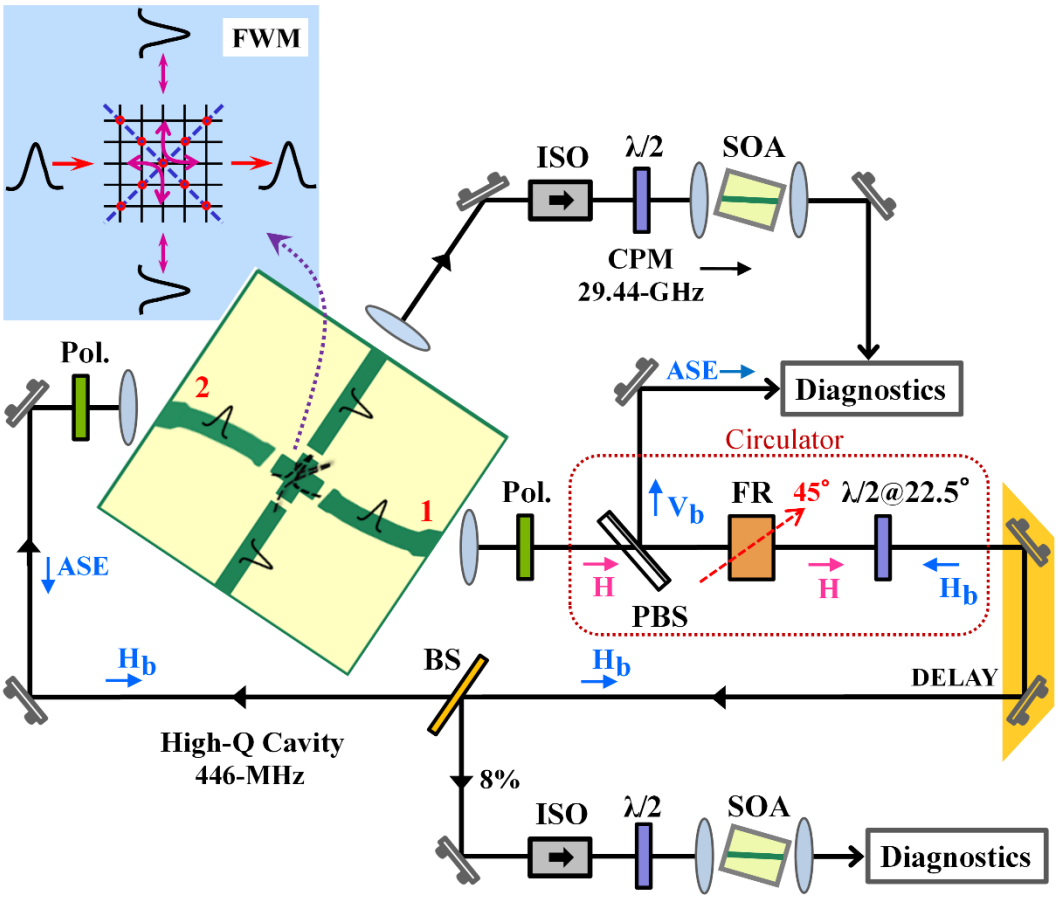

Figure 29: Schematic of the experimental setup to confirm four-wave mixing (FWM). The horizontal and vertical polarized light is shown using symbols H and V, respectively. The symbol H_b and V_b denote the polarization of the backward emitted ASE light in the counter-clockwise direction. The output ports of the external ring laser are marked as 1 and 2, respectively. ASE, amplified spontaneous emission; SOA, semiconductor optical amplifier; Pol, linear polarizer; PBS, polarizing beam splitter; FR, faraday rotator; BS, pellicle beam splitter; λ/2, half-wave plate; ISO, optical isolator.

The external high-Q ring laser is built using four gold coated external mirrors, with two mirrors mounted on a translation stage to control and precisely match the cavity length to a sub-harmonic of the CPM laser. The chosen cavity length corresponds to an FSR of 446 MHz, which is the 66th sub-harmonic of the CPM laser. A free space optical circulator is build inside the cavity with the help of a polarizing beam splitter (PBS), faraday rotator (FR) and a half-wave plate. This allows the cavity to operate unidirectional (clockwise) while simultaneously giving access to the ASE output emitted from the other facet in the counter-clockwise direction. Because of the non-reciprocity of the FR, this ASE component is vertically polarized and thus coupled out using the same PBS for analysis. Note that the light emitted from the semiconductor diode laser is horizontally polarized (TE) to begin with and care is taken to maintain that polarization by placing linear polarizer's at the outputs of the laser, which eliminates any residual vertical polarized light component arising from the minute tilt of the device while mounting. Passive mode-locking is achieved by applying a reverse bias voltage of -6.1 V on the common SA region, which is shared and kept constant with the SA of the CPM laser. The corresponding forward bias current used is 80 mA on each of the curved gain sections giving a pulsewidth of around 5 ps. As before, the reverse bias voltage and bias currents used in the experiment are carefully chosen to achieve simultaneous stable mode-locking of the external cavity laser and the CPM laser and to achieve optical spectral overlap of the two cavities.

3.2 Measurement and results

Injection locking is first verified by examining the RF and optical spectra of the CPM laser for reduction in the RF linewidth and for optical supermode suppression. As seen in Fig. 30(d), the reduction is not as drastic as observed previously, because of the

three-pulse interaction in the current setup as opposed to four pulses, though it's sufficient to achieve FWM and injection lock the CPM laser. The measurements before injection are taken by physically blocking the light inside the master ring cavity. Optical pulse injection is achieved by removing this beam block.

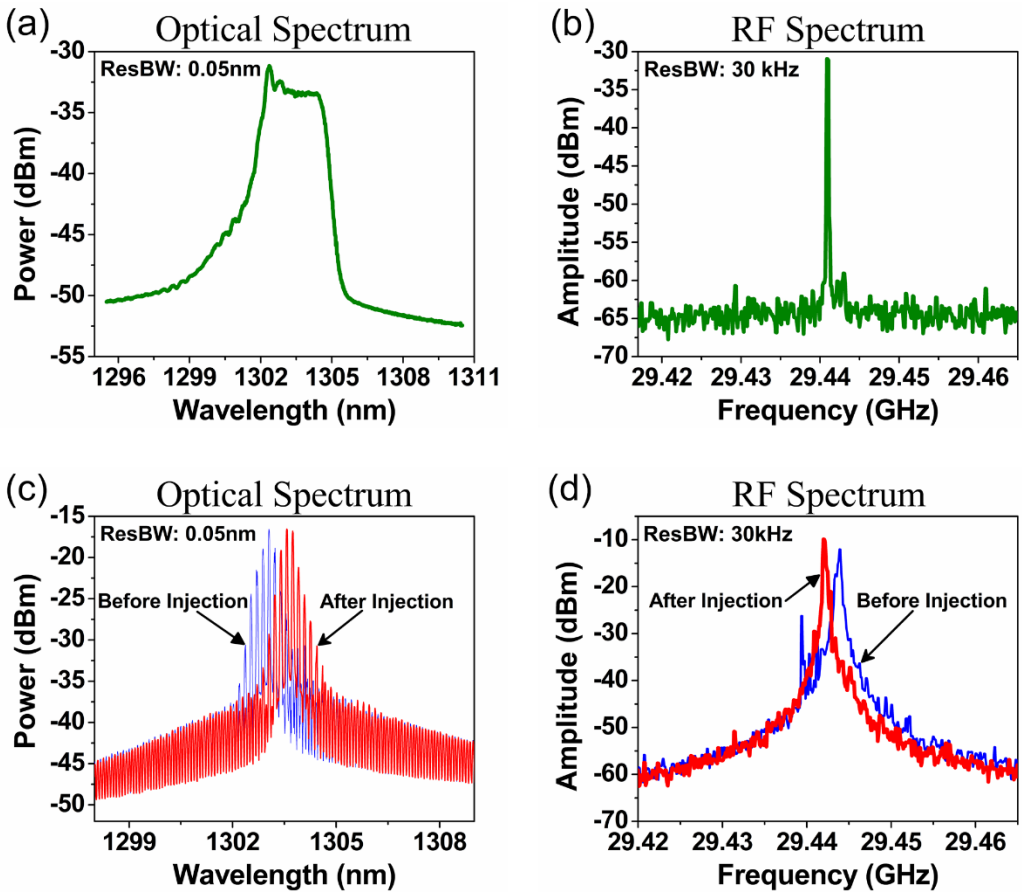

Figure 30: (a), (b): Typical spectra of the passively mode-locked high-Q external cavity (master) laser. (c), (d): Typical spectra of the passively mode-locked CPM (slave) laser before (in blue) and after (in red) optical injection.

Fig. 31(a) shows the optical spectrum of the backward propagating ASE output from port-2 of the external ring laser before and after injection. As seen in the figure, because of the back reflections from the circulator optics inside the external ring cavity, we do get leakage of the ring cavity lasing spectrum coupled to the ASE output, which though small can affect our measurements. The presence of the CPM light is then highlighted by examining the background subtracted ASE before and after injection locking. This is obtained by subtracting the two measured spectra shown in Fig. 31(a) displaying the result in Fig. 31(b). In the resultant difference spectra, the center of the spectrum clearly shows the diffracted spectra of the CPM laser which matches the location where the CPM mode-locked peak otherwise would fall.

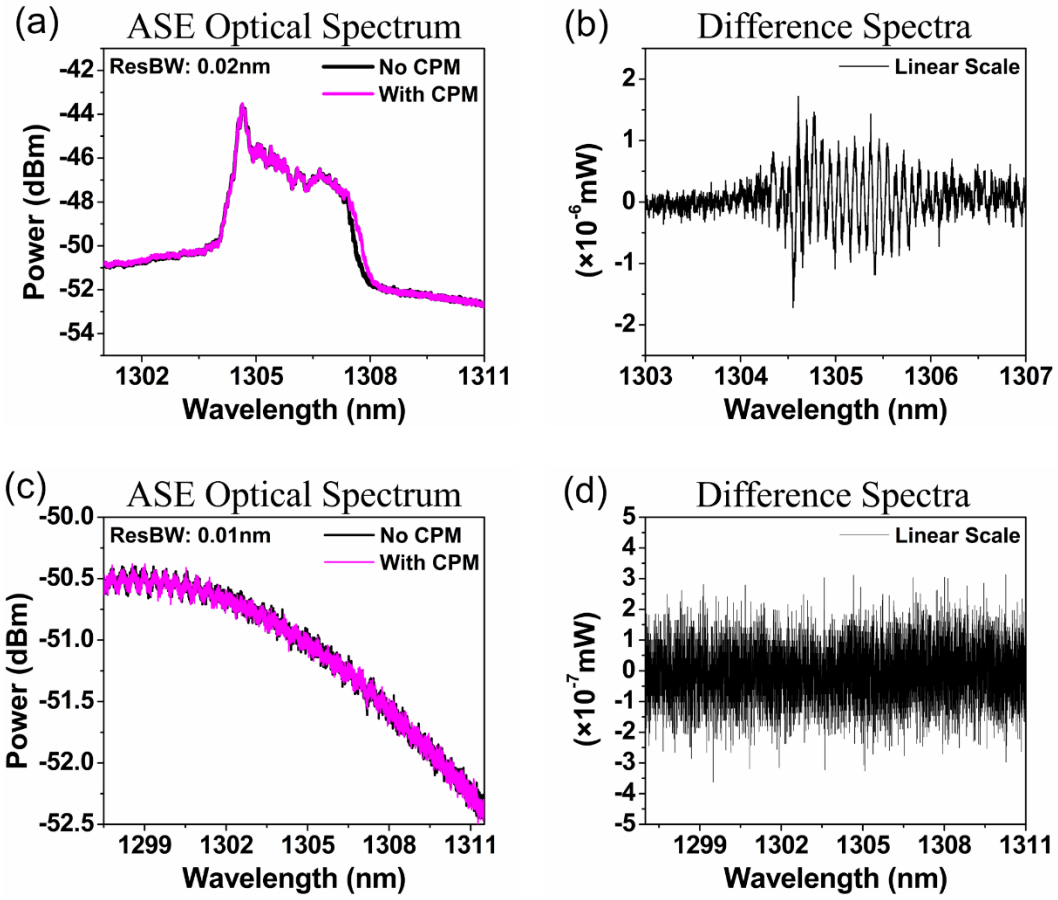

Figure 31: (a): Backward propagating ASE spectra from port-2 of the passively mode-locked high-Q external cavity (master) laser with and without injection of the CPM laser. Also seen is the back reflected leakage light from the intra-cavity optics superimposed on the ASE spectra. (b): Background subtracted spectra from Fig. 31(a), showing the diffracted CPM spectra present in port-2 due to FWM. (c): ASE spectra from port-2 of the master laser with port-1 physically blocked. (d): Background subtracted spectra from Fig. 31(c), with no residual CPM laser light observed in the absence of FWM.

It should be noted that the normal output of the 29.44 GHz CPM laser shows an axial mode spacing of 29.44 GHz. This is because there are two coherent pulse trains oscillating in a 14.72 GHz cavity, but temporally delayed by half-round trip. The resulting output thus displays an axial mode spacing of 29.44 GHz due to the spectral interference and resulting spectral modulation caused by the temporal delay of the two-pulse trains of ~ 34 ps. On the other hand, the output spectrum of the FWM signal shows an axial mode spacing of 14.72 GHz. This is because the two coherent pulse trains that possess axial modes at 14.72 GHz are diffracted simultaneously i.e., both pulse trains are temporally overlapped in time, resulting in observed spectra with axial modes at 14.72 GHz. Finally, it should be noted that the diffracted pulse occurs only every ~ 2 ns. This produces an additional spectral substructure at 446 MHz which is not spectrally resolved.

To make sure that the observed CPM light superimposed on top of the ASE output is only due to the aforementioned FWM and not due to any other linear scattering effect, we also measure the same ASE output from the ring cavity laser with and without CPM lasing while physically blocking port-1 before the PBS and keeping all the bias conditions the same. Any leakage of the CPM light into the ring cavity would then be seen in the measured optical spectrum. However, as seen in Fig. 31(d), the resultant subtracted spectrum with and without the port-1 blocked shows no residual CPM light, confirming that FWM is the primary mechanism for the injection locking in our design.

CHAPTER 4
IMPROVED STABILIZATION ARCHITECTURE

With an all passive stabilization architecture, the four-wave mixing technique is already shown to be very effective in reducing the long term frequency drift as well as the timing jitter of the high-repetition rate CPM laser. A QD based mode-locked design further offers reduced spontaneous emission rate and low threshold current density which leads to reduced noise. The extent of stabilization is, however, limited by the frequency and phase stability of the master ring laser which is passively mode- locked and thus still suffers from excess noise arising from the pulse-to-pulse timing fluctuations in the absence of any external synchronization [6], [7]. The optical phase noise and the timing jitter manifests themselves as the wide optical and RF linewidths of the master laser. In this chapter, we report on the performance of one scheme to overcome this limitation and help improve the design with jitter values that are more suitable and required for use in the future coherent communication systems.

4.1 Experimental setup

Fig. 32 illustrates the principle of the proposed scheme. The multi-section device consists of four gain sections and has a crossed saturable absorber (SA) section located at the symmetry center of the device. The monolithic CPM laser is formed from the cleaved facets of the linear gain sections. The two curved gain sections are part of an external high-Q ring cavity which is precisely built to a length corresponding to a subharmonic of the CPM slave laser. A fiberized lithium niobate ($LibNO_3$) intensity modulator is introduced to hybridly mode-lock and hence improve the phase stability of the master laser. The electro-optic modulator facilitates an all optical modulation, thus avoiding any electrical cross talk between gain sections which is otherwise seen when applying an RF modulation instead. By employing a longer cavity (compared to our previous work) and by using anti-reflection (AR) coatings on the curved gain facets further helps to improve the Q of the ring cavity which translates into an improved RF and optical stability of master laser. This improved stability is transferred to the monolithic CPM laser when the four pulses from the two crossed laser cavities meet in the common SA region. The pulse overlap leading to the formation of transient gratings (referred to degenerated FWM) with a resulting index of refraction at 45º to the face of the SA which causes the pulses to diffract from individual cavities into each other, essentially locking the CPM laser to the ring laser [17]. The principle of the method is confirmed by observing the narrowing of the RF and optical linewidths of the CPM laser giving rise to a stable ~ 30 GHz optical pulse train with pure spectral properties.

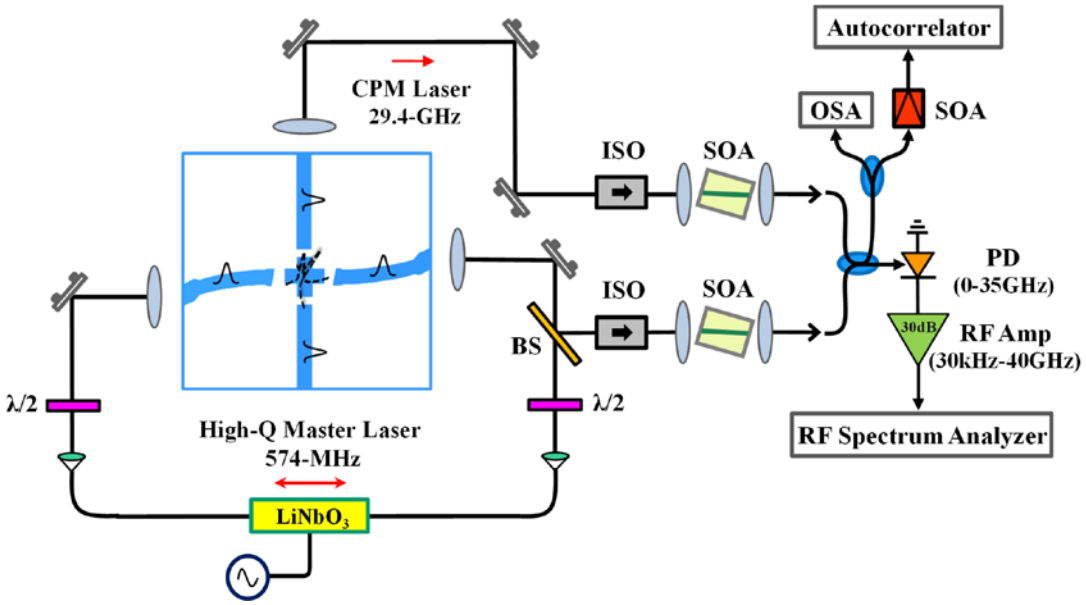

Figure 32: A schematic of the experimental setup. CPM: colliding pulse mode-locked slave laser, λ/2: half-wave plate, BS: beam splitter.

The monolithic gain chip is fabricated using the same commercially available quantum dot epi-wafer as described in chapter 2 and has the same waveguide design specifications. The gain chip is mounted on a gold coated copper stud and shares a thermo-electric (TEC) cooler with the external ring cavity for temperature control. The monolithic CPM slave laser has a total length of about 2.8 mm and under proper biasing conditions has two counter-propagating pulses which collide directly in the SA. As expected, this leads to a repetition rate of ~ 29.4 GHz which is twice the free spectral range (FSR) of the monolithic cavity. The master ring laser, with the two curved gain sections, is built using two external mirrors and a commercial mach-zehnder based fiberized $LiNbO_3$ intensity modulator. Aspheric lenses couple the light output from the facets into the lens collimators of the pigtailed $LiNbO_3$ modulator. The lens collimators are mounted on x, y, z stages to

control and precisely match the cavity length to a subharmonic of the CPM laser. Care is taken to match the left and right arms of the cavity for the pulses to meet inside the $LiNbO_3$ modulator in the bi-directional cavity. The chosen free-space length of the ring cavity is ~ 1.57 m, which corresponds to an FSR of 191 MHz. Half-wave plates inside the ring serve to match the polarization state of the $LiNbO_3$ modulator for maximum extinction and dominantly couple the TE mode back to the gain chip (since the QD laser lases in TE mode). In operation mode, all the gain sections are driven by constant current sources, while a voltage supply provides the reverse bias to the absorber section. Because of the common SA region, the reverse bias voltage and the bias currents used in the experiment are carefully chosen to achieve simultaneous stable mode-locking of the external cavity and the CPM laser. The output from the lasers is amplified using semiconductor optical amplifier (SOA), coupled into an SMF fiber, and finally split into a various number of instruments for diagnostics. The optical linewidths of the lasers are measured using the delayed self-heterodyne setup shown in Fig. 33.

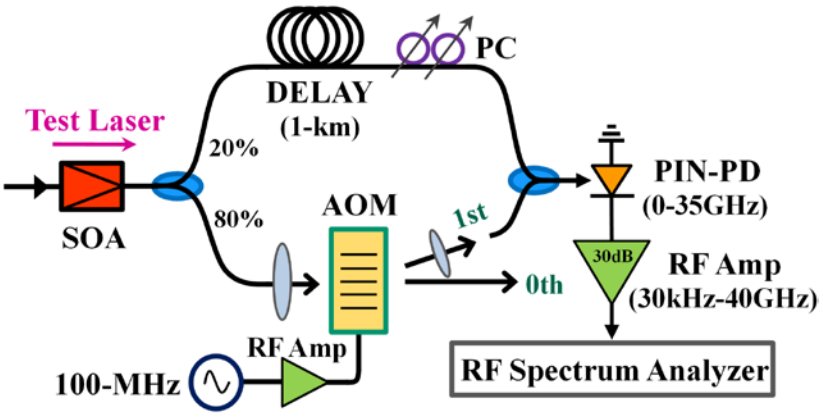

Figure 33: Delayed self-heterodyne setup used for optical linewidth measurement with 1-km of optical fiber.

The laser output is amplified using an SOA before going into an Mach-Zehnder interferometer (MZI). A splitting ratio of 80/20 is used to take care of the free-space to fiber coupling loss in case of the free space acousto-optic modulator (AOM) placed in one of the arms of the interferometer, operating at 100 MHz. The other port of the MZI is delayed by 1.0 km optical fiber which produces a uncorrelated beat tone at 100 MHz on an electrical spectrum analyzer and gives us a measure of the optical linewidth.

4.2 Measurement and results

Continuous wave (CW) operation of the high-Q ring laser is first confirmed by applying forward bias currents on each of the two curved gain sections, using DC probes. The QD based laser emits at 1.3 μm and has a threshold current of ~ 47 mA (applied on each gain section with no voltage on the absorber section and with $LiNbO_3$ modulator at transparency). Fundamental passive mode-locking at 191 MHz is observed with a reverse bias voltage of – 3.0 V ± 0.1 V on the SA. Because of the common crossed SA section, a SA voltage of -6.0 V (with a corresponding bias current of 100mA on each of the gain sections) is chosen, which gives a stable third harmonic mode-locking of the laser at 573.45 MHz and also results in a simultaneous stable mode-locking of the CPM laser. Hybrid mode-locking is achieved by applying an RF power of 20.5 dBm to the $LiNbO_3$ intensity modulator (from a sin-wave source at 573.45 MHz) and results in a much reduced phase noise compared to just passive mode-lock operation. The light is coupled out of the ring cavity using a pellicle beam splitter with a small reflectance (8%) to minimize the cavity loses and then amplified before photo-detection.

The spectral and the time domain outputs are shown in Fig. 34. A 50-GHz sampling scope triggered by the external microwave source clearly displays stable pulse train at the

laser frequency of 573.45 MHz, confirming that the third-order subharmonic hybrid mode-locking is indeed taking place synchronized to the microwave source. Also shown is the 10 dB optical linewidth of the ring laser. Since it is the result of a heterodyne beat of two combs, an average optical linewidth of ~3.74 MHz is measured. Taking into account the deconvolution factor of $2\sqrt{9}\ \Delta\nu$ for the 10 dB Lorentzian linewidth, yields a master laser linewidth of $\Delta\nu = 623$ KHz.

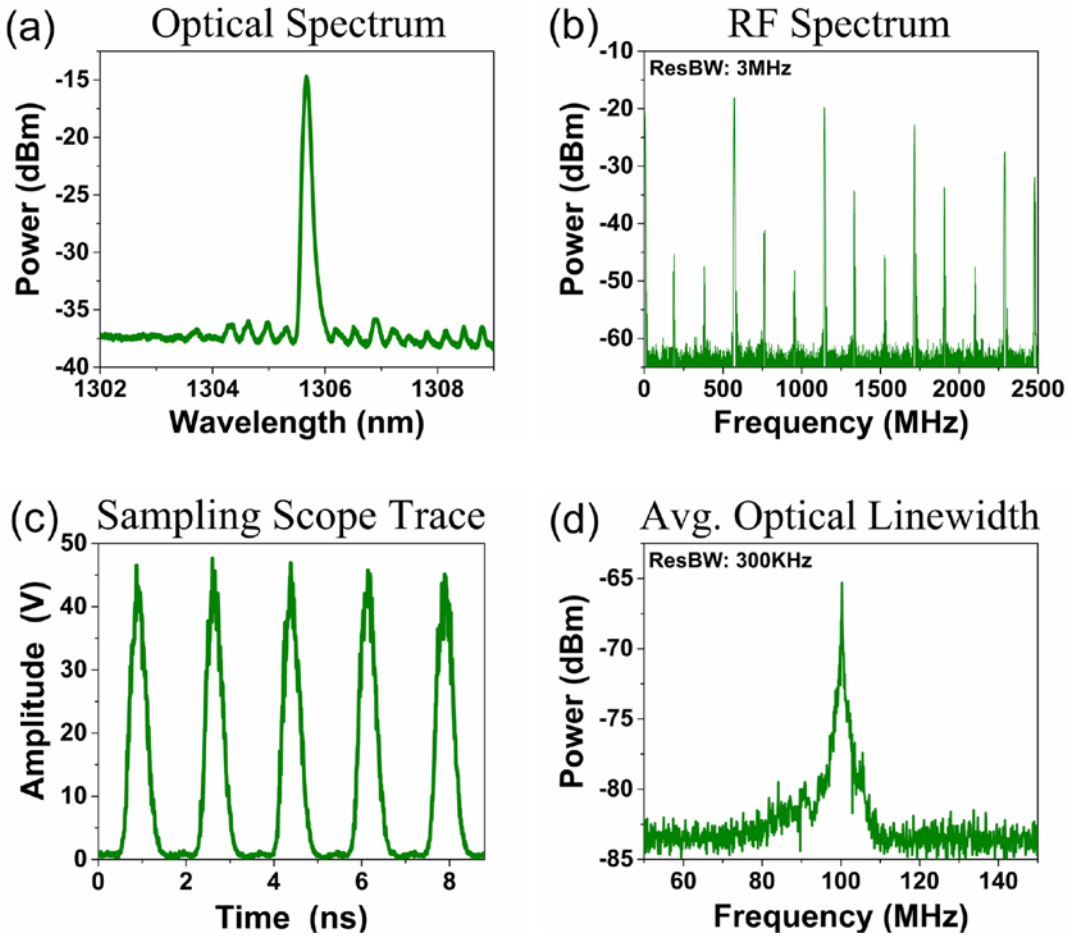

Figure 34: Spectra of the hybridly mode-locked (3rd harmonic mode-locking) high-Q external cavity (master) laser.

The CPM QD laser is passively mode-locked at the fundamental repetition rate of 29.4 GHz by applying a forward bias current of 46 mA on each of its gain sections and a reverse bias voltage of –6.0 V ± 0.1 V on the SA section. The threshold current of the laser is ~ 34 mA (applied on each of the linear gain sections with no voltage on the absorber section). Light is coupled out using an aspheric lens and then amplified using an SOA before going for diagnostics. The device temperature is tuned to ~ 19º C, to achieve optical spectral overlap of the two cavities which induces coupling and hence injection locking of the CPM laser to the high-Q external cavity. As seen in Fig. 36, the optical linewidth of the master ring laser does suffer when the bias conditions and temperature is tuned to achieve the optical spectral overlap with the CPM laser. In the near future, this can be easily circumvented by employing individual on-chip tuning elements such as heaters and Bragg gratings for the two lasers.

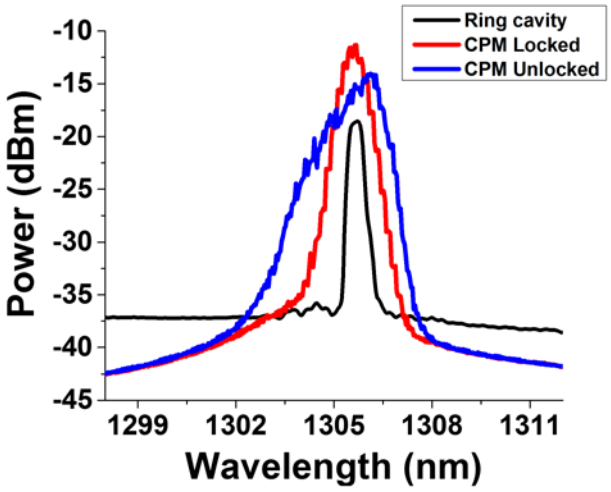

Figure 35: Optical spectral overlap of the slave and master laser achieved by tuning the device temperature (~18 º to 19 º C).

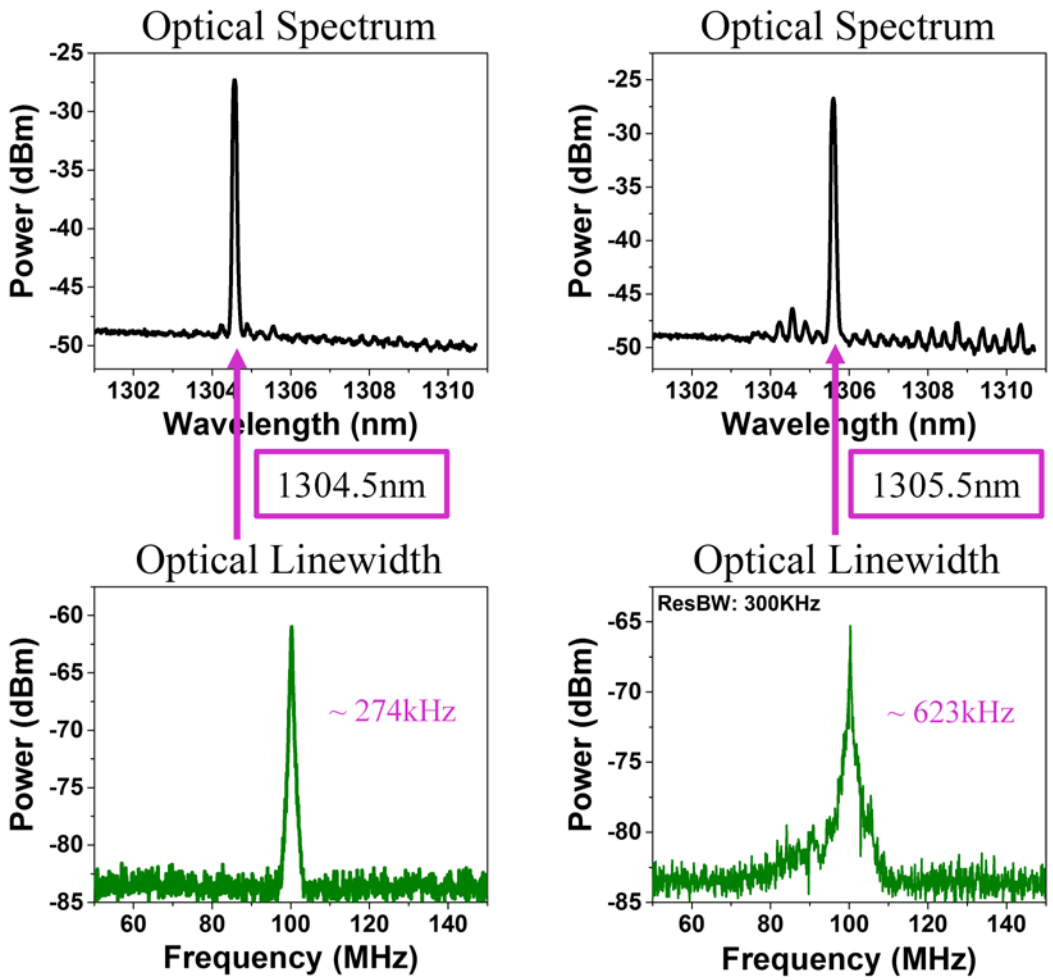

Figure 36: Optical linewidth variation of master ring-cavity with bias-conditions and temperature.

Fig. 37 (a)-(d) shows the optical and RF spectra of the passively mode-locked CPM laser before and after optical injection. As seen in Fig. 37(a), the CPM laser simultaneously operates with two sets of axial modes, (a characteristic of harmonic mode-locking) with an optical spectrum where the axial modes are spaced at the cavity FSR. In Fig. 37(b), the optical spectrum of the CPM laser is shown after injection locking. The previously observed, free running, passive mode- locked spectra, is now transformed to a spectra

showing an axial mode spacing of 29.4 GHz, which is a result of the injection process establishing coherency between the oscillating pulse pairs in the CPM lasers. The resulting coherence between the oscillating pulse pairs mandates that the axial modes of the injection locked CPM laser be observed at 29.4 GHz.

Fig. 37(c) shows the RF power spectra of the photodetected pulse train from the CPM laser, before and after injection locking. It is evident that the fundamental mode-locked frequency of the CPM laser has been pulled to the harmonic beat frequency of the injected master ring laser and the linewidth and the frequency fluctuation of the detected mm-wave carrier are drastically reduced. It should be noted that the RF linewidth is reduced from 4.64 MHz to 332 KHz, as measured 10 dB down from the carrier. This reduction in the RF linewidth is attributed to the injection locking process, which assists in establishing a well-defined phase relationship among the different axial modes in the optical domain, and is clearly evident, as manifested by more than 14-times reduction in the RF linewidth of the CPM laser. In addition, in Fig. 37(d), it is observed that the optical linewidth sees a ~ 5x reduction in the linewidth, from 5.40 MHz to 1.13 MHz (10 dB width, deconvolved) after injection locking. The reduction in the optical linewidth is a direct result of the CPM laser oscillation being injection locked by FWM and stabilized by the narrow axial modes from the master, hybridly mode-locked laser.

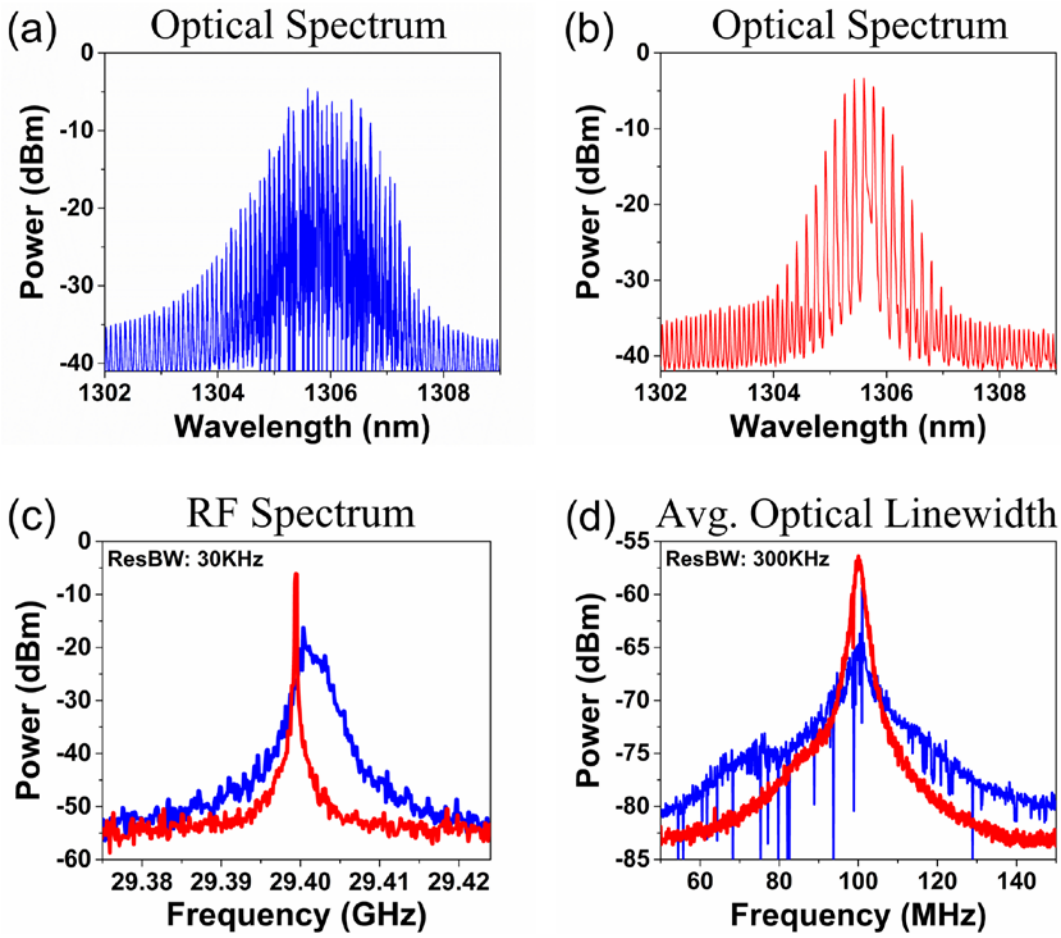

Figure 37: Spectra of the passively mode-locked CPM (slave) laser before (in blue) and after (in red) optical injection via four-wave mixing.

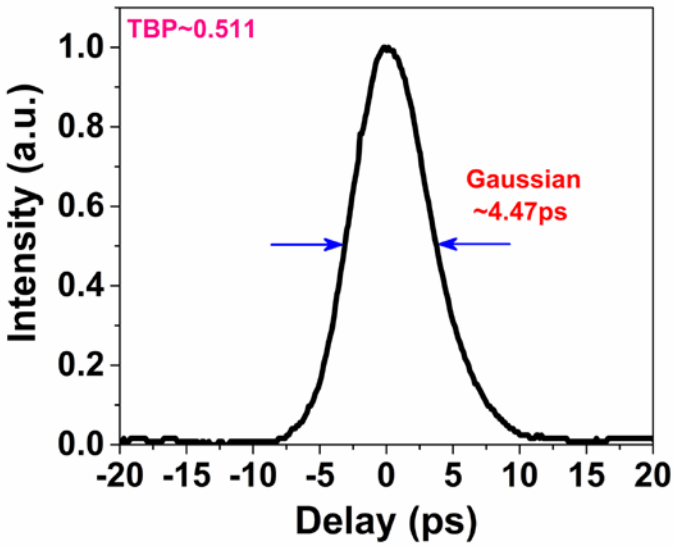

Figure 38: Autocorrelation trace and the measured pulse-width of the CPM laser.

The pulse width of the CPM laser is measured using an intensity auto-correlator. Assuming a Gaussian pulse shape, the autocorrelation trace shown in Fig. 38 translates into a pulse width of 4.47 ps and is identical both with and without injection. The optical spectrum of the pulse has a FWHM of 0.65 nm at wavelength of 1306 nm. The time bandwidth product (TBP) is thus 0.511, which is 1.16 times the transform limit, indicating near transform-limited pulses directly from the monolithic CPM laser.

CHAPTER 5
FUTURE ALL MONOLITHIC DESIGN

Compared to bulk and fiber optic systems, a photonic integrated device design can offer improved performance and stability in a smaller footprint and at a lower cost. Research in recent years has successfully explored various silica-on-silicon and hybrid-silicon based architectures for ultralow-loss, high-density multilayer waveguide routing for macro-chip interconnects [28-32]. The emerging research has demonstrated its potential utilizing low cost, mature and mass productive CMOS processes and the ability to combine III-V materials with silicon through heterogeneous integration. The limited performance of passive silicon components (in terms of insertion loss and channel cross talk due to high-index contrast) has been overcome with the advent of low-loss Si_3N_4 waveguides offering propagation loss of less than 0.1dB/m [33].

In this section, we present a unique platform that combines III-V and silicon photonic components with ultralow-loss Si_3N_4 waveguides for all-monolithic integration of the novel four-wave mixing stabilized ultrafast optical pulse. The design can be realized using an on-chip electro-absorption (EA) modulator or by RF modulating the gain medium itself at a sub-harmonic of the monolithic CPM laser for achieving a stable optical pulse source. We illustrate both these designs with detailed schematics and corresponding reference work.

5.1 Using optical hybrid mode-locking

Since silicon is an indirect band gap material, integration of III-V gain media and silicon is explored. As shown by Mizrahi et al. at Skorpios Technologies [34], the QD gain media in our case can be embedded within a silicon on insulator (SOI) wafer, where the epitaxial QD material is metal-bonded directly onto the silicon substrate within a pit receptor site inside the SOI wafer. The metal bond would serve as the bottom electrical contact and would avoid the lattice mismatch issues of depositing III-V on silicon. An illustration of this method together with the device layout is shown in Fig. 39. The gap which is formed between the gain medium and the silicon can be reconstructed with a buried oxide layer or Si_3N_4. As seen in Fig. 39 and Fig. 40, an amorphous silicon or low-loss Si_3N_4 waveguide with identical cross-section to those in QD gain media would serve as an integrated coupler. The integrated coupler forms the connection between the III-V waveguides and the long Si_3N_4 waveguides of the high-Q cavity formed on SOI chip. The gain waveguides are angled as our previous design to suppress unwanted reflections within the cavity. All waveguide structures can be defined in a single photolithography step followed by etching, as demonstrated in [34]. For hybrid mode-locking the high-Q ring cavity, several modulator structures such as micro-ring modulators, electroabsorption modulators (EAM) and Mach-Zehnder modulators in hybrid silicon have been explored. Referring to table 5, (from ref. [35]) and looking at some of the listed parameters for each specific modulator, we feel an EAM modulator which avoids the sensitivity to temperature and fabrication variations of ring modulators and is compact compared to an MZI modulator would be an ideal choice for hybrid mode-locking the high-Q ring cavity in the

monolithic design. The low-loss EAM modulator on the hybrid silicon platform has already been demonstrated and can be realized as described in ref. [36].

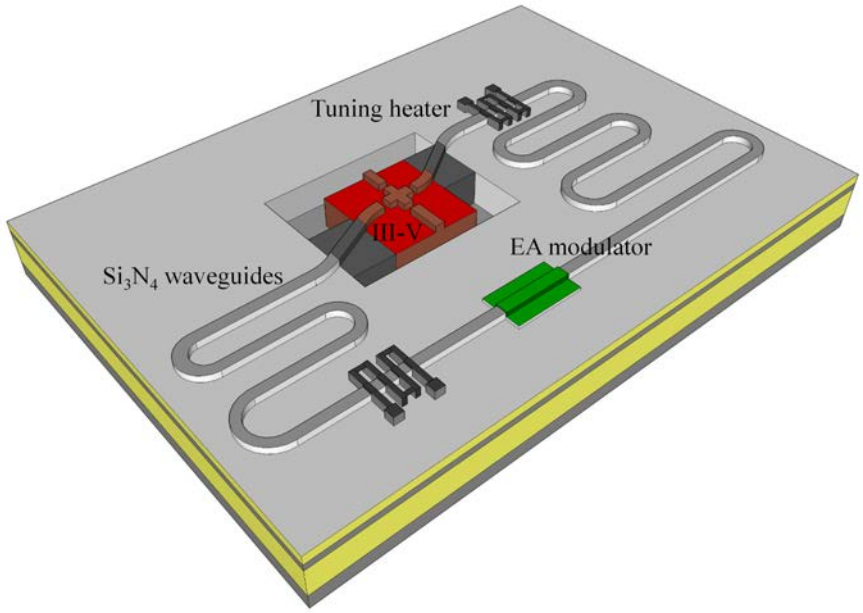

Figure 39: Illustration of all monolithically integrated novel design with epitaxial III-V gain material metal-bonded within SOI platform. The design would incorporate low-loss Si_3N_4 waveguides in the case of high-Q ring cavity which is then modulated with EA modulator (III-V based) for low-noise hybrid mode-locking.

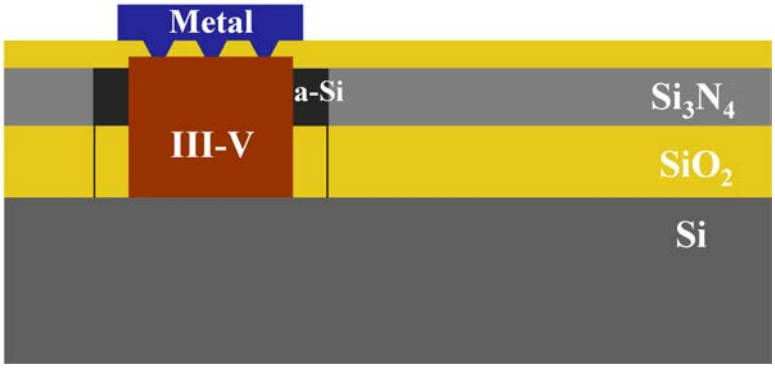

Figure 40: Cross-section view of the geometry of the future all monolithically integrated design.

Table 5: Comparison of silicon modulators (ref. [35]).

	Ring Modulator	EAM		MZM			
Group	Cornell	UCSB	MIT	UCSB	Intel	IBM	IEF
Platform	Si	Hybrid Si	SiGe	Hybrid Si	Si	Si	Si
ER (dB) and driven bias (V_{pp})	17 (1.8 V)	10 (5 V)	10 (7 V)	12 (4V)	>20 (6V)	6 to 10 (1.8V)	14 (10V)
Bandwidth (GHz)	—	16.0	1.0	8.0	20.0	—	8.0
ER(dB) at high freq.(Gb/s)	9dB at 12.5G*	11dB at 10G	—	6.38 at 10G	1dB at 30Gb	? at 10G*	—
Optical bandwidth (nm)	<1	30	15	> 100	> 75 nm	—	> 30 nm
$V_\pi L$ (Vmm)	—	—	—	2	40	0.36	50
length (um)	10	100	50	500	1000	100	4000
loss(dB)/device	—	3	14.8	3	5.4	12	5

5.2 Using RF hybrid mode-locking

Another way of realizing the all-monolithic optical pulse source on hybrid silicon platform is shown in Fig. 41. Instead of having the high-Q cavity in a ring format it can be also be built from linear Si_3N_4 waveguides (the waveguides can also be looped into a spiral if need be) with cleaved AR coated facets or by incorporating distributed Bragg reflector gratings together with heating elements at the end of the low-loss waveguides. This would provide an additional benefit whereby the external cavity can be tuned to match the lasing peak and longitudinal modes of the CPM laser for an optimal injection locking. This wavelength tuning with fabricated Bragg reflector gratings and heaters has already been demonstrated in ref. [34], [37]. The design can be further simplified by directly modulating the gain medium of the high-Q ring laser [38], [39] (with proper RF shielding) and thus avoiding the requirement of an additional EAM modulator.

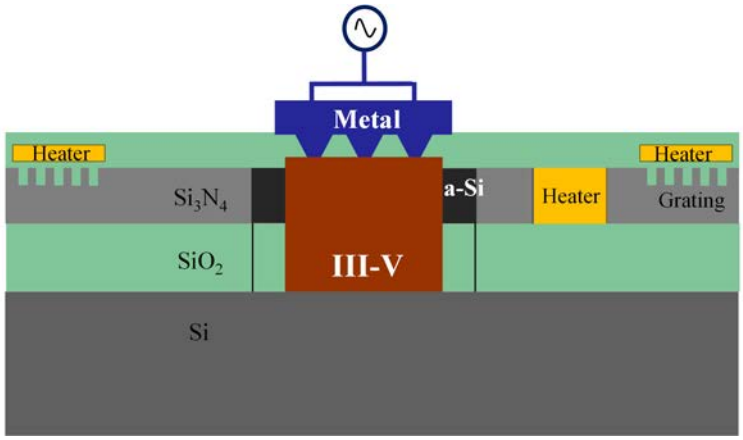

Figure 41: Cross-section view of the monolithic device with linear Si_3N_4 waveguides for the high-Q cavity and tunable distributed Bragg reflector (DBR) mirrors. The heaters together with DBR mirrors would serve as the phase tuning element for longitudinal optical mode overlap of the two crossed laser cavities for optimal injection locking.

CHAPTER 6
CONCLUSION

In summary, we have proposed and demonstrated a novel method of stabilizing high-repetition rate monolithic mode-locked diode lasers by purely optical means. As a first demonstration, an external high-Q master laser is used to injection lock an orthogonally coupled passively mode-locked monolithic CPM slave laser. Coupling between the crossed orthogonal laser cavities is achieved through four-wave mixing in the common monolithically integrated saturable absorber, which results in the locking and hence reduction of the timing jitter as well as the long-term frequency drift of the slave laser. In the initial all passive stabilization architecture, with both master and slave lasers passively mode-locked, a stable 30 GHz optical pulse train is generated with more than 10 dB reduction in the RF noise level at 20 MHz offset. The RF tone width is reduced by almost 5-times (from 24.35 MHz to 4.88 MHz) measured 30 dB down from the carrier and close to 3-times reduction of the 10 dB average optical linewidth (from 8 MHz to 3 MHz) is observed. Four-wave mixing process is subsequently investigated and experimentally confirmed to be the primary mechanism responsible for the interaction and locking of the CPM laser. Other linear scattering effects, which are predicted to be small are also investigated and found be negligible. The stabilization architecture of the novel coupled cavity laser is further improved by employing optical hybrid mode-locking and increasing the Q of the master laser cavity (using a longer cavity and AR coating the laser facets), which results in dramatic reduction in the optical and RF linewidths of the master ring laser. This higher stability translates into more than 14-times reduction (from 4.64 MHz to 332 KHz) in the 10dB RF linewidth and almost 5-times reduction in the 10dB optical linewidth

(from 5.40 MHz to 1.13 MHz) of the injection locked slave laser, confirming the effectiveness of the novel technique for all-on-chip stability transfer.

With the novel techniques recently demonstrated, such as active-passive waveguide integration and long low-loss passive waveguides (in III-V/Silicon), in the near future the narrow linewidth CPM laser employing the new FWM technique can be fabricated with the high-Q cavity in an all-monolithic architecture. With the resulting stabilized pulse train, this ultra-compact and ultrashort optical source would be attractive for use in the forthcoming photonic access networks employing technologies such as dense wavelength-division multiplexing (DWDM) and ultra-high speed time division multiplexing (OTDM).

APPENDIX A
C++ CODE USED FOR MASK LAYOUT

```
define waveguide {

#include "ldata.h" #include <stdlib.h> #include <math.h>

void  WaveguideMacro ( void )

 {  LPoint       Polygon [ 100 ];

   /*****General_Variables along x,y*****/

  double  X,Y,XE;

  double  Ltot, Wtot, Width, Lsa, Wsa, Lgap, Gap_Cen, Gap_Angle,Gap_Angle1,

        L1, L1tap, Le, Lcur, L2, L2tap, Wtap;    /***Wtap is Width after tapered***/

   /*****Start_Points(0,y)****/

  double  y_start;

   /*****Torus_Variables******/

  double  x_Torus, y_Torus, R, R_In, R_Out,Torus_Angle,Start_Angle, Stop_Angle,

        delta_x, delta_y, R2, R2_In, R2_Out, R5, R5_In, R5_Out;

   /*****"Taper+L1" Variables******/

  double       Rotate,

              x0,y0,x1,x2,x3,x4,x5,x6,y1,y2,y3,y4,y5,y6,

              rot_x1,rot_x2,rot_x3,rot_x4,rot_x5,rot_x6,

              rot_y1,rot_y2,rot_y3,rot_y4,rot_y5,rot_y6;

  double       Pi = 3.1415926535897938, hund = 100 * 1000, Tipsep = 150*1000;
```

```
  double      Add = 10*1000, Add_sa = 20*1000, Sep = 20*1000;
  double      Polygon_Points4, Polygon_Points6;


  LCell       Cell_Draw   = LCell_GetVisible ( );
  LFile       File_Draw   = LCell_GetFile ( Cell_Draw );
  LPoint      Translation = LCursor_GetPosition ( );
  LObject     Torus, Torus1, Torus2, Torus3;
  /*************************************************************************/
if(LLayer_Find(File_Draw, "Grid Layer") == NULL)
   { LDialog_AlertBox("There is no Grid Layer layer.
    \nMake sure Grid Layer is in the layer map!"); return;}
if(LLayer_Find(File_Draw, "Layer 0") == NULL)
   {LDialog_AlertBox("There is no Layer 0 layer.
    \nMake sure Layer 0 is in the layer map!"); return; }
  int i, j ;            /* i is row,  j is colum */
  #define k 8          /* k is how many row?   i=k */
  double array[k][14]={
```

```
/***************** QD TS(2.5mm) start****************/
/* (j=0)  (j=1)  Ltot(j=2)  Lsa(j=3)  w_sa(j=4)  L_gap(j=5)  L1(j=6)   L1tap(j=7)
    Wg(j=8)  Le(j=9)  Angle(j=10)   Ltap2(j=11)  L2(j=12)  w_tap(j=13) */
   { 0,  1,  2500,  280,  7,  15,  30,  80,  5,  0,  7,  70,  30,  7},
   { 0,  2,  2500,  280,  7,  15,  30,  80,  5,  0,  7,  70,  30,  7},
   { 0,  3,  2500,  280,  7,  15,  30,  80,  5,  0,  7,  70,  30,  7},
   { 0,  4,  2500,  280,  7,  15,  30,  80,  5,  0,  7,  70,  30,  7},
   { 0,  5,  2500,  280,  7,  15,  30,  80,  5,  0,  7,  70,  30,  7},
   { 0,  6,  2500,  280,  7,  15,  30,  80,  5,  0,  7,  70,  30,  7},
   { 0,  7,  2500,  280,  7,  15,  30,  80,  5,  0,  7,  70,  30,  7},
   { 0,  8,  2500,  280,  7,  15,  30,  80,  5,  0,  7,  70,  30,  7},
            /***************** QD TS(2.5mm) end****************/
          };


double v[14];
for (i=0; i<=k-1; i++) {
  for (j=0; j<=13; j++)
    { v[j]=array[i][j]; }
    Wtot = 600*1000;  Polygon_Points4 = 4;  Polygon_Points6 = 6;
```

```
X = 1000*v[0];  Y = Wtot*( v[1] - 1 );       /* Column start point */

Ltot = 1000 * ( v[2] );   Lsa = 1000 * ( v[3] );  Wsa = 1000 * ( v[4] );

Lgap = 1000 * ( v[5] );  Gap_Cen = Lsa + Lgap/2 ;

Gap_Angle1 = 8 * (Pi/180);  Gap_Angle = 8 * (Pi/180);   /* 8 degree */

L1 = 1000 * ( v[6] );  L1tap = 1000 * ( v[7] );  Width  = 1000 * ( v[8] );

Le = 1000 * ( v[9] );

Torus_Angle = (v[10])*(Pi/180); /***Equals to Lcur_Angle***/

L2tap = 1000 *  ( v[11] );  L2 = 1000 *  ( v[12] );  Wtap = 1000 *  ( v[13] );

Lcur = Ltot-(Lsa+Lgap+L1+L1tap+Le+L2tap+L2);

y_start = (200 * 1000) ;      /**SA(Center) [Start point  i.e. (0,y)]**/

R = Lcur/sin(Torus_Angle);  R_In = R - (Width/2);  R_Out = R + (Width/2);

Start_Angle = 270;  Stop_Angle = Start_Angle + (Torus_Angle)*180/Pi;

x_Torus = X + Lsa + Lgap + L1 + L1tap + Le;  y_Torus = Y + y_start + R ;

    /************* "Ltap2+L2" and Its Rotation_Variables*************/

x0 = x_Torus + Lcur;  y0 = Y + y_start + R*(1-cos(Torus_Angle)) ;

x1 = x0;  y1 = y0 - (Width/2);     x2 = x1 + L2tap;  y2 = y1 - ((Wtap-Width)/2);

x3 = x2 + L2 + Add;  y3 = y2;     x4 = x3;  y4 = y0 + Width/2 + ((Wtap-Width)/2);

x5 = x2;  y5 = y4;     x6 = x1;  y6 = y0 + Width/2;      Rotate = Torus_Angle;
```

```
/*** translate from (x0,y0) to (0,0), rotate and then translate to (x0,y0)***/

rot_x1 = ( (x1-x0)*cos(Rotate) - (y1-y0)*sin(Rotate) ) + x0;

rot_y1 = ( (x1-x0)*sin(Rotate) + (y1-y0)*cos(Rotate) ) + y0;

rot_x2 = ( (x2-x0)*cos(Rotate) - (y2-y0)*sin(Rotate) ) + x0;

rot_y2 = ( (x2-x0)*sin(Rotate) + (y2-y0)*cos(Rotate) ) + y0;

rot_x3 = ( (x3-x0)*cos(Rotate) - (y3-y0)*sin(Rotate) ) + x0;

rot_y3 = ( (x3-x0)*sin(Rotate) + (y3-y0)*cos(Rotate) ) + y0;

rot_x4 = ( (x4-x0)*cos(Rotate) - (y4-y0)*sin(Rotate) ) + x0;

rot_y4 = ( (x4-x0)*sin(Rotate) + (y4-y0)*cos(Rotate) ) + y0;

rot_x5 = ( (x5-x0)*cos(Rotate) - (y5-y0)*sin(Rotate) ) + x0;

rot_y5 = ( (x5-x0)*sin(Rotate) + (y5-y0)*cos(Rotate) ) + y0;

rot_x6 = ( (x6-x0)*cos(Rotate) - (y6-y0)*sin(Rotate) ) + x0;

rot_y6 = ( (x6-x0)*sin(Rotate) + (y6-y0)*cos(Rotate) ) + y0;

        /*******************Device Size*******************

Polygon [ 0 ] = LPoint_Set ( X + 0,    Y +   0  );

Polygon [ 1 ] = LPoint_Set ( X + Ltot, Y +   0  );

Polygon [ 2 ] = LPoint_Set ( X + Ltot, Y + Wtot );

Polygon [ 3 ] = LPoint_Set ( X + 0,    Y + Wtot );

LPolygon_New ( Cell_Draw, LLayer_Find ( File_Draw, "Grid Layer" ),
```

```
                Polygon, 1*Polygon_Points4);

            /**********************SA************************** */

        Polygon [ 0 ] = LPoint_Set (X - Add_sa, Y + y_start - Wsa/2);

        Polygon [ 1 ] = LPoint_Set (X + Lsa - (Wsa/2)*tan(Gap_Angle1), Y + y_start - Wsa/2);

        Polygon [ 2 ] = LPoint_Set (X + Lsa + (Wsa/2)*tan(Gap_Angle1), Y + y_start +
Wsa/2);

        Polygon [ 3 ] = LPoint_Set (X -Add_sa, Y + y_start + Wsa/2);

        LPolygon_New ( Cell_Draw, LLayer_Find ( File_Draw, "Layer 0" ),

                Polygon, 1*Polygon_Points4);

          /**********************L1 + L1Tap**************************/

 Polygon [ 0 ] = LPoint_Set (X + Lsa + Lgap + (Wsa/2)*tan(Gap_Angle) ,Y + y_start -
Wsa/2);

 Polygon [ 1 ] = LPoint_Set (X + Lsa + Lgap + L1,Y + y_start - Wsa/2);

 Polygon [ 2 ] = LPoint_Set (X + Lsa + Lgap + L1 + L1tap,Y + y_start - Width/2);

 Polygon [ 3 ] = LPoint_Set (X + Lsa + Lgap + L1 + L1tap,Y + y_start + Width/2);

 Polygon [ 4 ] = LPoint_Set (X + Lsa + Lgap + L1,Y + y_start + Wsa/2);

 Polygon [ 5 ] = LPoint_Set (X + Lsa + Lgap - (Wsa/2)*tan(Gap_Angle),Y + y_start +
Wsa/2);

 LPolygon_New ( Cell_Draw, LLayer_Find ( File_Draw, "Layer 0" ),

          Polygon, 1*Polygon_Points6);
```

```
/**************************Le*****************************/
    Polygon [ 0 ] = LPoint_Set (X + Lsa + Lgap + L1 + L1tap,Y + y_start - Width/2);
    Polygon [ 1 ] = LPoint_Set (X + Lsa + Lgap + L1 + L1tap + Le,Y + y_start - Width/2);
    Polygon [ 2 ] = LPoint_Set (X + Lsa + Lgap + L1 + L1tap + Le,Y + y_start + Width/2);
    Polygon [ 3 ] = LPoint_Set (X + Lsa + Lgap + L1 + L1tap,Y + y_start + Width/2);
    LPolygon_New ( Cell_Draw, LLayer_Find ( File_Draw, "Layer 0" ),
            Polygon, 1*Polygon_Points4);
          /**********************Torus*****************************/
 LTorusParams tParams;
       tParams.ptCenter.x = x_Torus;
       tParams.ptCenter.y = y_Torus;
       tParams.nInnerRadius = R_In;
       tParams.nOuterRadius = R_Out;
       tParams.dStartAngle = Start_Angle;
       tParams.dStopAngle = Stop_Angle;
 Torus = LTorus_CreateNew(Cell_Draw, LLayer_Find ( File_Draw, "Layer 0" ),
&tParams);
 LTorus_GetParams(Torus, &tParams);
```

```
            /**********************Tap + L2***************************/
            Polygon [ 0 ] = LPoint_Set ( rot_x1, rot_y1 );
            Polygon [ 1 ] = LPoint_Set ( rot_x2, rot_y2 );
            Polygon [ 2 ] = LPoint_Set ( rot_x3, rot_y3 );
            Polygon [ 3 ] = LPoint_Set ( rot_x4, rot_y4 );
            Polygon [ 4 ] = LPoint_Set ( rot_x5, rot_y5 );
            Polygon [ 5 ] = LPoint_Set ( rot_x6, rot_y6 );
        LPolygon_New ( Cell_Draw, LLayer_Find ( File_Draw, "Layer 0" ),
                    Polygon, 1*Polygon_Points6);
  }   // for loop end here;
      LCell_MakeVisible (Cell_Draw);  LCell_HomeView(Cell_Draw);
  }   // WaveguideMacro end here
void  waveguide_macro_register ( void )
       { LMacro_BindToHotKey ( KEY_F10, "QD_1Col_TS(2.5mm)_Curved_array",
         "WaveguideMacro" ); }
}    // define waveguide end here
waveguide_macro_register();
```

APPENDIX B
PECVD RECIPE FILES

Cyclotene.prc

[_INI_HEADER_]

Version=1

[Step_001]

Description=, StepType=12004 INITIAL, Name=CYCLOTEN

DefaultPumps=0, InitPumpdown=1

Temp1Out=0, Temp2Out=0, Temp3Out=0, Temp4Out=0

BasePressure=0.04, PressureExp=5, HoldTime=10, Chamber=1, LogConfig=

[Step_002]

Description=Flush, StepType=12005 PROCESS

ChannelNames=BCL3,N2,O2,CHF3,HE,CF4, Channels=0,90,0,0,0,0

Pressure=500, PressureExp=0, ProcessPump=0, Terminate=0

MaxStepTime=60, MaxEndTime=0

OverEtch=0, OverEtchTime=0, OverEtchPercent=0

RFControls=1,0, RFSetpoints=0,0,0,0,0,0, RFConfig=1, RFGenerators=0,0,0,0

EndptMethod=0, HeliumCooling=0, Angstroms=0

AMNMode=0, AMNTuneSetpoints=0, AMNLoadSetpoints=0, DepRate=

[Step_003]

Description=, StepType=12007 EVAC

ProcessPump=1, PumpTime=10, BasePressure=0.03, PressureExp=5

[Step_004]

Description=Gas Stabilization, StepType=12005 PROCESS

ChannelNames=BCL3,N2,O2,CHF3,HE,CF4, Channels=0,0,10,0,0,5

Pressure=50, PressureExp=0, ProcessPump=1

Terminate=0, MaxStepTime=60, MaxEndTime=0

OverEtch=0, OverEtchTime=0, OverEtchPercent=0

RFControls=1,0, RFSetpoints=0,0,0,0,0,0, RFConfig=1, RFGenerators=0,0,0,0

EndptMethod=0, HeliumCooling=0, Angstroms=0, AMNMode=0

AMNTuneSetpoints=0, AMNLoadSetpoints=0, DepRate=

[Step_005]

Description=Cyclotene Etch, StepType=12005 PROCESS

ChannelNames=BCL3,N2,O2,CHF3,HE,CF4, Channels=0,0,10,0,0,5

Pressure=50, PressureExp=0, ProcessPump=1, Terminate=3

MaxStepTime=60, MaxEndTime=0

OverEtch=0, OverEtchTime=0, OverEtchPercent=0

RFControls=1,0, RFSetpoints=100,0,0,0,0,0, RFConfig=1, RFGenerators=0,0,0,0

EndptMethod=0, HeliumCooling=0, Angstroms=0

AMNMode=0, AMNTuneSetpoints=0, AMNLoadSetpoints=0, DepRate=

[Step_006]

Description=, StepType=12007 EVAC

ProcessPump=1, PumpTime=10, BasePressure=0.04, PressureExp=5

[Step_007]

Description=, StepType=12006 PURGE

Pressure=1000, PressureExp=0, Pump=0, PTime=10

RFConfig=1, RFControls=1,0, RFSetpoints=0,0,0,0,0,0

[Step_008]

Description=, StepType=12010 END

FinalPump=1, BasePressure=10, PressureExp=2, HoldTime=10, Vent=0

Prremove.prc

[_INI_HEADER_]

Version=1

[Step_001]

Description=, StepType=12004 INITIAL, Name=PRREMOVE

DefaultPumps=0, InitPumpdown=1

Temp1Out=0, Temp2Out=0, Temp3Out=0, Temp4Out=0

BasePressure=0.03, PressureExp=5, HoldTime=10, Chamber=1, LogConfig=

[Step_002]

Description=Gas Stablization, StepType=12005 PROCESS

ChannelNames=BCL3,N2,O2,CHF3,HE,CF4, Channels=0,0,50,0,50,0

Pressure=300, PressureExp=0, ProcessPump=0, Terminate=0

MaxStepTime=10, MaxEndTime=0

OverEtch=0, OverEtchTime=0, OverEtchPercent=0

RFControls=1,0, RFSetpoints=0,0,0,0,0,0, RFConfig=1, RFGenerators=0,0,0,0

EndptMethod=0, HeliumCooling=0, Angstroms=0

AMNMode=0, AMNTuneSetpoints=0, AMNLoadSetpoints=0, DepRate=

[Step_003]

Description=RF on, StepType=12005 PROCESS

ChannelNames=BCL3,N2,O2,CHF3,HE,CF4, Channels=0,0,50,0,50,0

Pressure=300, PressureExp=0, ProcessPump=0, Terminate=3

MaxStepTime=60, MaxEndTime=0, OverEtch=0, OverEtchTime=0,OverEtchPercent=0

RFControls=1,0, RFSetpoints=100,0,0,0,0,0, RFConfig=1, RFGenerators=0,0,0,0

EndptMethod=0, HeliumCooling=0

Angstroms=0, AMNMode=0, AMNTuneSetpoints=0, AMNLoadSetpoints=0, DepRate=

[Step_004]

Description=, StepType=12007 EVAC

ProcessPump=0, PumpTime=10, BasePressure=30, PressureExp=2

[Step_005]

Description=, StepType=12006 PURGE, Pressure=1000, PressureExp=0

Pump=0, PTime=10, RFConfig=1, RFControls=1,0, RFSetpoints=0,0,0,0,0,0

[Step_006]

Description=, StepType=12010 END

FinalPump=0, BasePressure=50, PressureExp=2, HoldTime=10, Vent=0

REFERENCES

[1] Th. Udem, R. Holzwarth, and T. W. Hänsch, "Optical Frequency Metrology", *Nature* 416, pp. 233-237, 2002.

[2] P. J. Delfyett, I. Ozdur, N. Hoghooghi, M. Akbulut, J. Davila-Rodriguez, and S. Bhooplapur, "Advanced Ultrafast Technologies Based on Optical Frequency Combs", *IEEE Journal of Selected Topics in Quantum Electronics*, vol. 18, no. 1, pp. 258-274, 2012.

[3] M. G. Thompson, A. R. Rae, M. Xia, R. V. Penty, and I. H. White, "InGaAs Quantum-Dot Mode-Locked Laser Diodes", *IEEE Journal of Selected Topics in Quantum Electronics*, vol. 15, no. 3, pp.661-672, 2009.

[4] E. U. Rafailov, M. A. Cataluna, and W. Sibbett, "Mode-Locked Quantum-Dot Lasers", *Nature Photonics* 1, 395, 2007.

[5] X. Huang, A. Stintz, H. Li, L. F. Lester, J. Cheng and K. J. Malloy, "Passive Mode-Locking in 1.3 μm Two-Section InAs Quantum Dot Lasers", *Applied Physics Letters*, vol. 78, no. 19 , pp. 2825-2827, 2001.

[6] D. J. Derickson, P. A. Morton, J. E. Bowers, and R. L. Thornton, "Comparison of Timing Jitter in External and Monolithic Cavity Mode-Locked Semiconductor Lasers", *Applied Physics Letters*, vol. 59, no.26 , pp. 3372-3374, 1991.

[6] L. Drzewietzki, S. Breuer, and W. Elsäßer, "Timing jitter reduction of passively mode-locked semiconductor lasers by self- and external-injection: numerical description and experiments," *Optics Express*, vol. 21, no. 13, pp. 16142-16161, Jun, 2013.

[7] D. J. Derickson, “Multi-Section Mode-Locked Semiconductor Lasers,” *Ph.D. dissertation*, University of California, Santa Barbara, 1992.

[8] X. S. Yao, L. Davis and L. Maleki, “Coupled Optoelectronic Oscillators for Generating Both RF Signal and Optical Pulses”, *Journal of Lightwave Technology*, vol. 18, no.1, pp. 73-78, 2000.

[9] B. K. Mathason, and P. J. Delfyett, “Pulsed Injection Locking Dynamics of Passively Mode-Locked External-Cavity Semiconductor Laser Systems for All-Optical Clock Recovery”, *Journal of Lightwave Technology*, vol. 18, no.8 , pp. 1111-1120, 2000.

[10] S. Arahira and Y. Ogawa, “Synchronous Mode-Locking in Passively Mode-Locked Semiconductor Laser Diodes Using Optical Short Pulses Repeated at Subharmonics of the Cavity Round-Trip Frequency”, *IEEE Photonics Technology Letters*, vol. 8, no. 2, pp. 191-193, 1996.

[11] P. Del´Haye, A. Schliesser, O. Arcizet, T. Wilken, R. Holzwarth and T. J. Kippenberg, “Optical Frequency Comb Generation from a Monolithic Microresonator”, *Nature* 450, pp. 1214, 2007.

[12] S. Arahira, and Y. Ogawa, “480-GHz Sub-harmonic Synchronous Mode-locking in a Short-cavity Colliding-pulse Mode-locked Laser Diode”, *IEEE Photonics Technology Letters*, vol. 14, no. 4, pp. 537-539, 2002.

[13] Y. K. Chen, and M. C. Wu, “Monolithic Colliding-pulse Mode-locked Quantum-well Lasers”, *IEEE Journal of Quantum Electronics*, vol. 28, no. 10, pp. 2176-2185, 1992.

[14] P. Vasil'ev, *Ultrafast Diode Lasers: Fundamentals and Applications* (London: Artech House, 1995).

[15] F. Quinlan, S. Ozharar, S. Gee, and P. J. Delfyett, "Harmonically Mode-locked Semiconductor-based Lasers as High Repetition Rate Ultralow Noise Pulse Train and Optical Frequency Comb Sources," *Journal of Optics A: Pure and Applied Optics*, vol. 11, no. 10, 2009.

[16] D. Kühlke, W. Rudolph, and B. Wilhelmi, "Influence of Transient Absorber Gratings on the Pulse Parameters of Passively Mode-Locked CW Dye Ring Lasers, *Applied Physics Letters*, vol. 42, no. 4, pp. 325-327, 1983.

[17] J. Buchert, R. Dorsinville, P. Delfyett, S. Krimchansky, and R. R. Alfano, "Determination of Temporal Correlation of Ultrafast Laser Pulses Using Phase Conjugation", *Optics Communications*, vol. 52, no. 6, pp. 433-437, 1985.

[18] H. K. Lee, V. Loyo-Maldonado, B. C. Qiu, K. L. Lee, C. Shu, S. Pinches, I. G. Thayne, A. C. Bryce, and J. H. Marsh, "Efficient Direct Locking of Colliding Pulse Mode-Locked Lasers on Semi-Insulating Substrate at 1.5 μm", *IEEE Photonics Technology Letters*, vol. 14, no. 8, pp. 1049-1051, 2002.

[19] S. Arahira, S. Kutsuzawa and Y. Ogawa, "Extreme Timing Jitter Reduction of a Passively Mode-Locked Laser Diode by Optical Pulse Injection", *IEEE Journal of Quantum Electronics*, vol. 35, no. 12, pp. 1805-1811, 1999.

[20] H. C. Bao and H. F. Liu, "Amplitude Noise of Subharmonically Hybrid Mode-Locked Pulses Generated From a Monolithic Semiconductor Laser", *IEEE Photonics Technology Letters*, vol. 14, no. 1, pp. 6-8, 2002.

[21] M. T. Choi, J. M. Kim, W. Lee, and P. J. Delfyett, "Ultralow Noise Optical Pulse Generation in an Actively Mode-locked Quantum-dot Semiconductor Laser", *Applied Physics Letters*, vol. 88, no. 13, pp. 131106-131108, 2006.

[22] M. Laemnlin, G. Fiol, C. Meur, M. Kuntz, F. Hopfer, A. R. Kovsh, N. N. Ledentsov, and D. Bimberg, "Distortion-free Optical Amplification of 20-80 GHz Modelocked Laser Pulses at 1.3 μm using Quantum Dots", *Electronics Letters,* vol. 42, no. 12, pp.697-699, 2006.

[23] C. E. Zah, R. Bhat, S. G. Menocal, N. Andreadakis, F. Favire, C. Caneau, M. A. Koza, and T. P. Leee, "1.5 μm GaInAsP Angled-Facet Flared-Waveguide Traveling-Wave Laser Amplifiers, *IEEE Photonics Technology Letters*, vol. 2, no. 1, pp. 46-47, 1990.

[24] I. P. Kaminow, G. Eisenstein, and L. W. Stulz, "Measurement of the Modal Reflectivity of an Antireflection Coating on a Superluminescent Diode", *IEEE Journal of Quantum Electronics*, vol. 19, no. 4, pp. 493-495, 1983.

[25] D. J. Derickson, *Fiber Optic Test and Measurement* (Prentice Hall, New Jersey, 1998), p.185.

[26] C. van Dam, F. P. G. M. van Ham, F. H. Groen, J. J. G. M. van der Tol, I. Moerman, and M. K. Smit, "Compact InP-based Waveguide Crossings with Low Crosstalk and Low Loss", *in Conf. Proc. Integrated Photonics Research (Boston)*, vol. 6, paper IMH-1, 1996.

[27] M. G. Daly, P. E. Jessop, and D. Yevick, "Crosstalk Reduction in Intersecting Rib Waveguides", *Journal of Lightwave Technology*", vol. 14, no. 7, pp.1695-1698, 1996.

[28] Chen J., R. G. Broeke, Y. Du, Jing Cao, N. Chubun, P. Bjeletich, F. Olsson, S. Lourdudoss, R. Welty, C. Reinhardt, P. L. Stephan, and S. J. B. Yoo, "Monolitically integrated InP-based photonic chip development for O-CDMA systems," *IEEE Journal of Selected Topics in Quantum Electronics*, vol. 11, no. 1, pp. 66-77, Jan. 2005.

[29] S. T. S. Cheung, F. M. Soares, J. H. Baek, B. Gaun, F. Olsson, S. Lourdudoss, and S. J. B. Yoo, "Monolithically integrated 10-GHz ring colliding pulse mode-locked laser for on-chip coherent communications," *in Conf. Proc. Conference on Lasers and Electro-Optics (CLEO)*, paper CW1N.8, May 2012.

[30] G. Li, J. Yao, Y. Luo, H. Thacker, A. Mekis, X. Zheng, I. Shubin, J. Lee, K. Raj, J. E. Cunningham, and A. V. Krishnamoorthy, " Ultralow-loss, high-density SOI optical waveguide routing for macrochip interconnects," *Optics Express*, vol. 20, no. 11, pp. 12035-12039, May 2012.

[31] J. F. Bauters, M. J. R. Heck, D. John, D. Dai, M. Tien, J. S. Barton, A. Leinse, R. G. Heidmeman, D. J. Blumenthal, and J. E. Bowers, "Ultra-low-loss high-aspect-ratio Si_3N_4 waveguides," *Optics Express*, vol. 19, no. 4, pp. 3163-3174, Feb. 2011.

[32] M. Piels, J. F. Bauters, M. L. Davenport, M. J. R. Heck, and J. E. Bowers, " Low-loss silicon nitride AWG demultiplexer heterogeneously integrated with hybrid III-V/silicon photodetectors", *Journal of Lightwave Technology*, vol. 32, no. 4, pp. 1-7, Feb. 2014.

[33] J. F. Bauters, M. J. R. Heck, D. D. John, J. S. Barton, C. M. Bruinink, A. Leinse, R. G. Heidmeman, D. J. Blumenthal, and J. E. Bowers, "Planar waveguides with less than

0.1 dB/m propagation loss fabricated with wafer bonding," *Optics Express*, vol. 19, no. 24, pp. 24090-24101, Nov. 2011.

[34] E. Marchena, T. Creazzo, S. B. Krasulick, P. K. L. Yu, D. V. Orden, J. Y. Spann, C. C. Bilvin, J. M. Dallesasse, P. Varangis, R. J. Stone, and A. Mizrahi, "Integrated tunable CMOS laser for Si photonics", *in conference proceedings OFC/NFOEC Postdeadline Papers*, paper PDP5C.7, 2013.

[35] H. Chen, Y. Kuo and J. E. Bowers, "High speed silicon modulators", *in conference proceedings OECC 2009*, paper ThG1, Hong Kong, Jul. 2009.

[36] Y. Tang, H. Chen, S. Jain, J. D. Peters, U. Westergren, and J. E. Bowers, " 50Gb/s hybrid silicon traveling-wave electroabsorption modulator", *Optics Express*, vol. 19, no. 7, pp. 5811-5816, Mar. 2011.

[37] I. A. Avrutsky, D. S. Ellis, A. Tager, H. Anis, and J. M. Xu, "Design of widely tunable semiconductor lasers and the concept of binary superimposed gratings (BSG's)", *IEEE Journal of Quantum Electronics*, vol. 34, no. 4, pp. 729-741, Apr. 1998.

[38] J. Kim, and P. J. Delfyett, " Interband optical pulse injection locking of quantum dot mode-locked semiconductor laser", *Optics Express*, vol. 16, no. 15, pp. 11153-11161, Jul. 2008.

[39] E. Sarailou, A. Ardey, and P. J. Delfyett, "Low noise ultrashort pulse generation by direct RF modulation at 22 GHz from an AlGaInAs multiple quantum-well laser at 1.55 μm", *IEEE Photonics Technology Letters*, vol. 24, no. 17, pp. 1561-1563, Sep. 2012.